Fundamentals of reservoir surface energy as related to surface properties, wettability, capillary action, and oil recovery from fractured reservoirs by spontaneous imbibition

DE-FC26-03NT15408

Semi-Annual Report
07/01/2006 – 12/31/2006

Norman R. Morrow, Principal Investigator
Herbert Fischer
Yu Li
Geoffrey Mason
Douglas Ruth
Peigui Yin
Shaochang Wo

February 2007
Re-submitted March 2007

Submitted by:
Chemical & Petroleum Engineering
University of Wyoming
Dept. 3295, 1000 E. University Ave
Laramie, WY 82071

Disclaimer

This report was prepared as an account of work sponsored by an agency of the United States Government. Neither the United States Government nor any agency thereof, nor any of their employees, makes any warranty, express or implied, or assumes any legal liability or responsibility for the accuracy, completeness, or usefulness of any information, apparatus, product, or process disclosed, or represents that its use would not infringe privately owned rights. Reference herein to any specific commercial product, process, or service by trade name, trademark, manufacturer, or otherwise does not necessarily constitute or imply its endorsement, recommendation, or favoring by the United States Government or any agency thereof. The views and opinions of authors expressed herein do not necessarily state or reflect those of the United States Government or any agency thereof.

ABSTRACT

The objective of this project is to increase oil recovery from fractured reservoirs through improved fundamental understanding of the process of spontaneous imbibition by which oil is displaced from the rock matrix into the fractures. Spontaneous imbibition is fundamentally dependent on the reservoir surface free energy but this has never been investigated for rocks. In this project, the surface free energy of rocks will be determined by using liquids that can be solidified within the rock pore space at selected saturations. Thin sections of the rock then provide a two-dimensional view of the rock minerals and the occupant phases. Saturations and oil/rock, water/rock, and oil/water surface areas will be determined by advanced petrographic analysis and the surface free energy which drives spontaneous imbibition will be determined as a function of increase in wetting phase saturation. The inherent loss in surface free energy resulting from capillary instabilities at the microscopic (pore level) scale will be distinguished from the decrease in surface free energy that drives spontaneous imbibition.

A mathematical network/numerical model will be developed and tested against experimental results of recovery versus time over broad variation of key factors such as rock properties, fluid phase viscosities, sample size, shape and boundary conditions. Two fundamentally important, but not previously considered, parameters of spontaneous imbibition, the capillary pressure acting to oppose production of oil at the outflow face and the pressure in the non-wetting phase at the no-flow boundary versus time, will also be measured and modeled. Simulation and network models will also be tested against special case solutions provided by analytic models.

In the second stage of the project, application of the fundamental concepts developed in the first stage of the project will be demonstrated. The fundamental ideas, measurements, and analytic/numerical modeling will be applied to mixed-wet rocks. Imbibition measurements will include novel sensitive pressure measurements designed to elucidate the basic mechanisms that determine induction time and drive the very slow rate of spontaneous imbibition commonly observed for mixed-wet rocks. In further demonstration of concepts, three approaches to improved oil recovery from fractured reservoirs will be tested; use of surfactants to promote imbibition in oil wet rocks by wettability alteration: manipulation of injection brine composition: reduction of the capillary back pressure which opposes production of oil at the fracture face.

TABLE OF CONTENTS

INTRODUCTION

Objectives

The long-range objective of this project is to improve oil recovery from fractured reservoirs through improved fundamental understanding of the process of spontaneous imbibition by which oil is displaced from the rock matrix into the fractures. Spontaneous imbibition is fundamentally dependent on the surface energy. An initial objective is to determine the surface energy and relate the dissipation of surface energy to the mechanism of spontaneous imbibition. A parallel objective is to model the mechanism of spontaneous imbibition by a combination of network analysis and numerical modeling. Also fundamentally important, but not previously considered, parameters of spontaneous imbibition, the capillary pressure acting to oppose production of oil at the outflow face and the pressure in the non-wetting phase at the no-flow boundary (in effect within oil in the non-invaded zone of the rock matrix) versus time, will also be measured and compared with values predicted by the mathematical model. The next objective is to measure surface energy and related spontaneous imbibition phenomena for mixed-wettability rocks prepared by adsorption from crude oil. The dissipation of surface free energy must then be related to oil production at mixed-wet conditions. The final objective is to apply the results of the project to improved oil recovery from fractured reservoirs in three ways: reduction of the capillary force that opposes oil production at the fracture face; change in wettability towards increased water wetness; identification of conditions where choice of invading brine composition can give improved recovery.

TASKS

Budget period 1, July 1, 2003 through June 30, 2005 – Ideas and Concept development: Fundamentals of Spontaneous Imbibition

Task 1. *Work of displacement and surface free energy.* Obtain complementary sets of capillary pressure drainage and imbibition data and data on changes in rock/brine, rock/oil, and oil/brine interfacial areas with change in saturation for drainage and imbibition for at least two rock types (sandstone and carbonate). Determine free-energy/work-of-displacement efficiency parameters for drainage and imbibition for at least two rock types so that changes in rock/wetting phase/non-wetting phase surface areas can be closely estimated from capillary pressure measurements.

Task 2. *Imbibition in simple laboratory and mathematical network models.* Study imbibition in at least three simple tube networks that can be modeled analytically to establish and/or confirm fundamental aspects of the pore scale mechanism of dynamic spontaneous imbibition with special emphasis on determining how spontaneous imbibition is initiated and the key factors in how the saturation profile develops with time. Incorporate rules developed from laboratory measurements on relatively simple networks into the design of a computational network model. Use the network model to obtain an account of the mechanism by which imbibition is initiated, the saturation profile is developed, and the rate of spontaneous imbibition in terms of the dissipation of surface free energy that accompanies change in saturation.

Task 3. *Novel observations on fluid pressures during imbibition and the mechanism of non-wetting phase production at the imbibition face.* Make novel observations on the imbibition

mechanism including details of the mechanism of oil production at the outflow rock face and the change in the non-wetting phase pressure at the no-flow boundary of the core during the course of spontaneous imbibition for at least 16 distinct combinations of rock/ fluid properties.

Task 4. *Network/numerical model and new imbibition data.* Develop a numerical simulator specifically designed for spontaneous imbibition. Incorporate the network model to obtain a network/numerical model that includes matching the measured pressure in the non-wetting phase at the no-flow boundary, and the pressure that opposes production of oil at the open rock face. Imbibition data will be obtained for at least 10 rocks with over six-fold variation in permeability, and at least 6 orders of magnitude variation in viscosity ratio, and at least 10 variations in sample size, shape, and boundary conditions.

Task 5. *Comparison with similarity solutions.* Compare results given by simulation with special case analytic results given by similarity solutions for spontaneous imbibition for at least five distinct cases of rock and fluid properties.

Budget Period 2, July 1, 2005 through June 30, 2008 - Demonstration of concept: Application to mixed wettability rocks and improved oil recovery from fractures reservoirs.

Task 6. *Rock preparation and Work of displacement and surface areas*
Obtain a range of rock types and identify and obtain crude oils that induce stable mixed wettability. Prepare at least 25 rocks with mixed wettability through crude oil/brine/rock interactions. Determine work of displacement for drainage and imbibition and measure the variation in rock/brine, rock/oil, and oil/brine interfacial areas during the course of drainage and imbibition for at least two examples of mixed wettability.

Task 7. *Novel imbibition measurements on mixed-wet rock and network models.* Obtain, for at least six mixed-wet rocks, spontaneous imbibition data that includes measurements of the non-wetting phase pressure at the no-flow boundary, observations on the capillary pressure that resists production at the open rock face.

Task 8. *Application of network/numerical model to mixed wet rocks.* Use network models to relate dissipation of surface energy to rate of spontaneous imbibition and to account for the frequently observed induction time prior to the onset of spontaneous imbibition into mixed wettability rocks.

Task 9. *Increased oil recovery by spontaneous imbibition.* The mechanism of increased recovery from mixed wet rocks by use of surfactants that promote spontaneous imbibition by favorable wettability alteration will be investigated for at least four distinct examples of crude oil/brine/rock/surfactant combinations. The mechanism of increased recovery by manipulation of brine composition will be investigated for at least four crude oil/brine/rock combinations. Addition of very low concentration surfactants to the imbibing aqueous phase will be explored as a means of increasing the rate of oil recovery by reducing the capillary forces which resist production of oil at the fracture face. At least twelve combinations of rock and fluid properties including both very strongly wetted and mixed wet rocks will be tested.

EXECUTIVE SUMMARY

Significant advances have been made in understanding the mechanism of spontaneous imbibition. Surface area measurements show that the conversion of work to surface energy for drainage is very inefficient (~25% for sandstones and ~16% for carbonates). Driving pressures for spontaneous imbibition have been determined for a range of initial surface energy states given by strongly water-wet and mixed-wet rock at different levels of initial water saturation. An analytic solution has been developed for countercurrent imbibition which gives close agreement with experimental results for a wide range of conditions. The complex mechanism countercurrent imbibition for non-axially symmetric tubes has been investigated by novel experimental techniques and explained quantitatively through analysis of menisci of complex shape.

PROGRESS BY TASK - BUDGET PERIOD 2

Task 6. *Rock preparation and Work of displacement and surface areas*

Introduction of Rock preparation and Work of displacement and surface areas

A novel approach to measurement of pressures acting during imbibition has been applied to strongly water wet rocks and to rocks with wettability altered by aging with crude oil. The study included mixed wet rocks obtained by aging with crude oil in the presence of an initial water saturation. Results for strongly water-wet rocks with and without initial saturation provide a reference for wettability alteration induced by aging with crude oil. Imbibition rates for mixed-wet rocks was generally much slower than for strongly wetted conditions. Surface free energy at the start of imbibition and capillary pressures acting during imbibition must be correspondingly low. The measured pressures are considered for most practical purposes to be the maximum pressures that can be generated by spontaneous imbibition.

Experimental

Rocks

All tested cores were selected from high permeability Berea sandstone (D=3.2~3.8 cm, L=6.2 cm~6.6cm, ϕ=22 %~22.7%, K=0.86 μm^2 to1.07 μm^2). All low permeability core segments were cut from Texas Leuders limestone (D=3.88 cm, L=1. 6 cm, ϕ=16 %, K=0.002 μm^2). The low permeability core was selected so that it would be partially drained by influx of oil from the main core but still remain below the percolation threshold for oil production.

Oils and brine.

Refined oil was used in the very strongly water wet tests. The oil was cleaned by flow through a mixture of silica gel and alumina. Cottonwood crude oil was selected for wettability control because it gives moderate wettability alteration. The density of Cottonwood crude oil is 0.8874 (20^oC) and the viscosity is 24.1 *Pa.s*. The brine (10,000 *ppm* NaCl) had a viscosity of 0.00102 *Pa.s* and density of 0.998 (20^oC). Initial water saturations were established with tap water to give the contrast in conductivity needed to detect the location or distance of advance of the brine

along the core. The interfacial tension between Cottonwood crude oil and the brine is 29.7 mN/m.

Initial water saturation

Initial water saturation, S_{wi} was established by flow of Viscous Mineral oil (VMO) (commercial name is "Extra Heavy Oil", viscosity of 173.0 cP). Tests were run for Soltrol 220 refined oil (viscosity of 0.0038 *Pa.s*) with S_{wi} of 17.9% and 25.2%. If mineral oil was chosen as the nonwetting phase, the VMO used to establish the initial water saturation was displaced by Soltrol 220 (total injection volume was 5 PV). For tests with crude oil, the viscous oil was displaced by 5 PV decalin followed by injection of 5 PV of crude oil through each end of the core. For the two MXW tests with Cottonwood crude oil (viscosity of 0.0241 *Pa.s*) S_{wi} was 16.8 % and 25.3 %. Cores were aged with Cottonwood crude oil at 75^{o}C for 10 days. The initial saturation was established with low ionic strength brine so that the advance of the imbibition front of the invading brine along the core could be tracked from the change in electrical conductivity between electrodes spaced along the core. Any permeability damage due to salinity contrast will be minimal because the main segment has high permeability and the amount of brine that enters the core is very restricted. In some cases the distance of advance was detected by slicing the core along its length and using electrodes to locating a sharp rise in electrical resistivity.

Composite cores

Composite cores were prepared by butting the main core segment containing oil (either with or without an initial water saturation) against a low permeability segment that was fully saturated with brine. Core properties are given in Table 6-1. A slurry formed from oil and powder (crushed core) was placed between the butted faces to ensure hydraulic contact. The cores are sealed except for the low permeability end face. The closed end of the high permeability segment is connected to a sensitive pressure transducer. The open face of the core is then exposed to brine as shown in Fig. 6-1. The approach is to measure the end pressure, $P_{end,}$ for one-face-open cores during restricted COUCSI. (Observed fluctuations (usually minor) in the pressure data are ascribed to diurnal variation in temperature and atmosphere pressure.) Further details are given with the results.

Cores initially saturated with mineral oil VSWW,S_{wi} =0

H6O(VSWW, S_{wi} =0)

The low permeability segment was a 2.351 *cm* long core of Berea sandstone with permeability of 0.065 μm^2.

Movement of the water front was detected by the onset of electrical conductivity when invading brine contacted a particular electrode. Results for test H6O are shown in Fig. 1. The end pressure rose quickly to 11 *kPa* but took a further 2.08 *days* to reach its highest value of 12.36 *kPa.* At that time, the front had penetrated 3.25 cm into the high *K* core segment (x_f/L_c =0.47) for the main core. The pressure was monitored for a further 1.8 days to confirm that a stable end pressure had been attained. No oil production was observed from the open face throughout the whole process. Thus the increase in saturation of the main segment was through exchange of water by oil in the contacting powder and the larger pores of the low permeability segment that connected to the region of contact between the two cores. At the end of the test, the main core was sawed open along its length for measurement of electrical conductivity from the butted face

to the front. The maximum advance of the interface was identified from sharp increase in electrical conductivity from the butted face to the electrode test point.

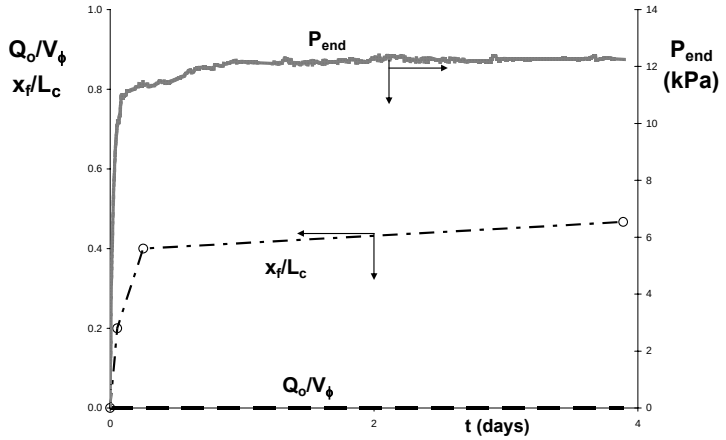

Fig. 6-1 Values of the end pressure, distance of invasion and oil production versus time for 1.067 μm^2 Berea sandstone core initially saturated with mineral oil. (Core H6O,VSWW,S_{wi} =0)

.

OW2(VSWW, S_{wi} =0)

The low *K* segment in Test OW2 was prepared as in Test OW2. The main segment was shorter (3.17 *cm*) than in Test OW2(6.97 *cm*). For restricted COUCSI, the end pressure rose to 13.7 *kPa* within 1 day and reached its highest value of 14.4 *kPa* after 2 *days* (Fig. 6-2). From resistivity measurements for electrode set along the core and also from pressure decline, the brine had penetrated the whole length of the main segment 3.3 *days* after the start of imbibition. The pressure then decreased to 12.550 *kPa* after a further half day.

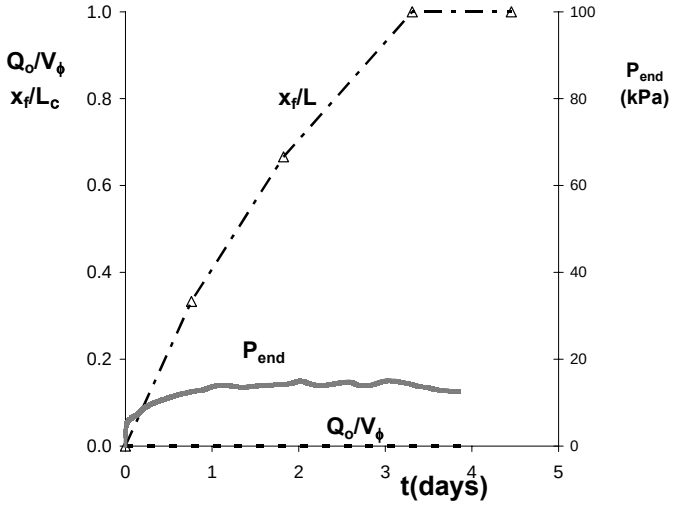

Fig. 6-2 Values of the end pressure, distance of invasion and oil production versus time for 0.964 μm^2 Berea sandstone initially saturated with mineral oil (S_{wi}=0). Core OW2,(VSWW, S_{wi} =0)

Cores initially saturated with crude oil CO,S_{wi} =0

HC4, CO,S_{wi} =0

Results for test H4C are shown in Fig. 6-3. The end pressure rose to 1.8 *kPa* within 15 minutes then slowly fell to 1.6 *kPa* after 2.9 hours. The drop may have been related to the presence of the thin layer of powdered core placed between the butted ends to ensure capillary contact. As confirmation of this explanation, the end tube was opened and the end pressure fell to zero. After closing the end, the end pressure rose to 1.6 *kPa* and recovered its initial value after 7.1 hours. At that time the onset of electrical conductivity when the brine front contacted a particular electrode showed that the front had penetrated 0.202 of the main core length (1.32 *cm*). The pressure was monitored for a further 22 *hours* to confirm that a stable end pressure had been attained. No oil production was observed from the open face throughout the test.

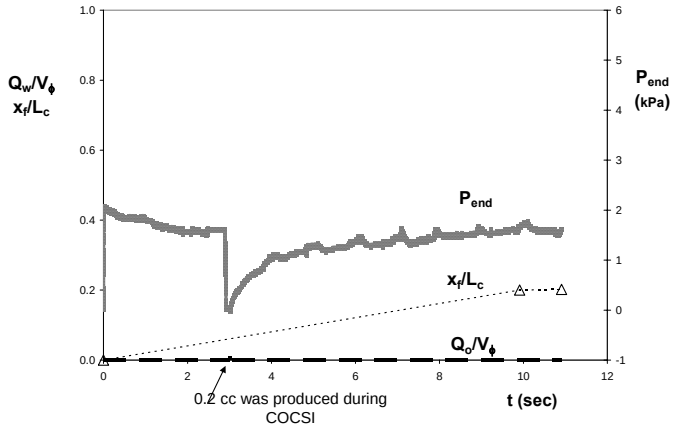

Fig. 6-3 The end pressure, distance of invasion and oil production for an aged core H4C initially saturated with Cottonwood crude oil (S_{wi}=0). No oil was produced. (HC4, CO,S_{wi} =0)

HE2, CO,S_{wi} =0%

The end pressure rose to a maximum value of about1.64 *kPa* after 16days. At this time the brine had already contacted the second electrode located at 0.2 (1.27 cm) of the main core length. No oil production was observed from the open face throughout the test.

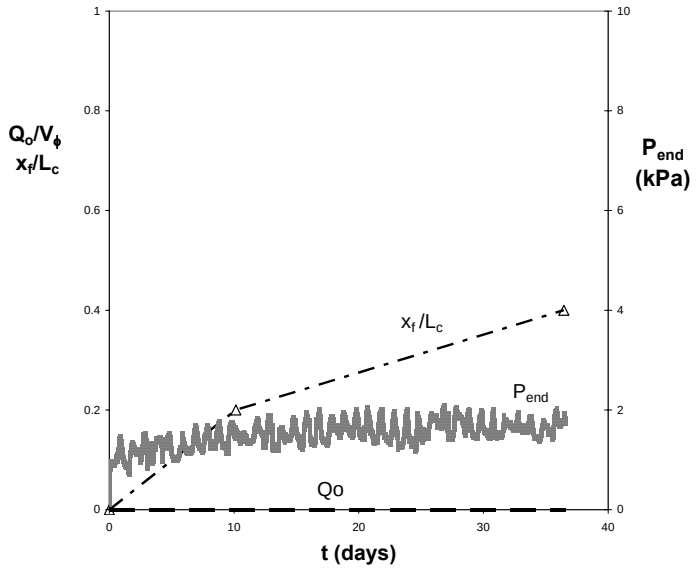

Fig. 6-4 The end pressure and distance of invasion for an aged core HE4 initially saturated with Cottonwood crude oil (S_{wi}=0). No oil production was observed from the open face of the low permeability core. (HE2, CO,S_{wi} =0)

Cores containing mineral oil and an initial water saturation. VSWW,S_{wi}

HB1, VSWW, S_{wi} = 17.9%

The end pressure rose to 1.7 *kPa* 0.8 days after the composite core was immersed in brine. Results for test HB1 are shown in Fig. 6-5. Then the end pressure gradually rose to about 4.7 *kPa*. The invading brine reached the dead end (5 days after the composite core had been immersed). The end pressure then slowly fell to about 2 *kPa* 30 days later.

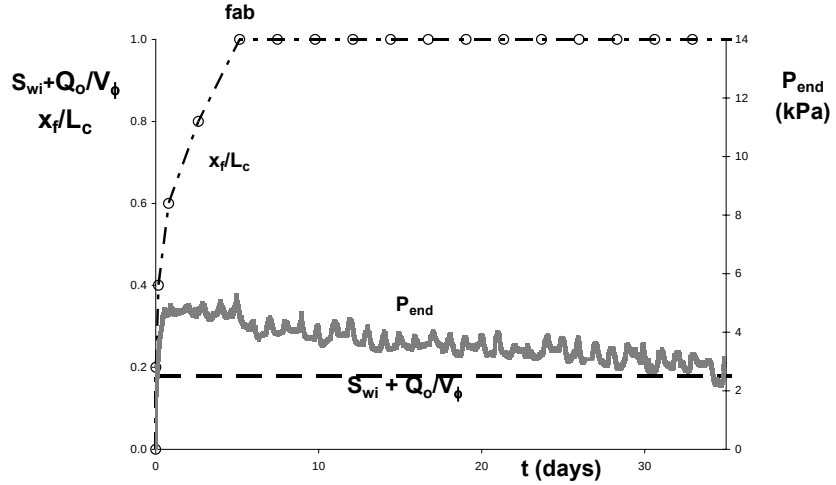

Fig. 6-5 The end pressure, distance of invasion and oil production for core HB1 (initially saturated with mineral oil, S_{wi}=17.9%).

HB3, VSWW,S_{wi} = 25 %

The semi-permeable segment was a 1.27 *cm* long segment of Texas Leuders limestone with permeability of 0.002 μm^2. The low K segment had been fully saturated by brine before being butted against the main segment, which contained 75% mineral oil and 25% tap water. Results for HB3 are shown in Fig. 6-6.

The end pressure rose to 3.25 *kPa* 0.9 days after the composite core was immersed in brine and then remained at 3.3 *kPa* until the front reached the dead end (4.5 days after the composite core had been immersed). The end pressure then slowly fell to about 0.15 *kPa* after 19 days.

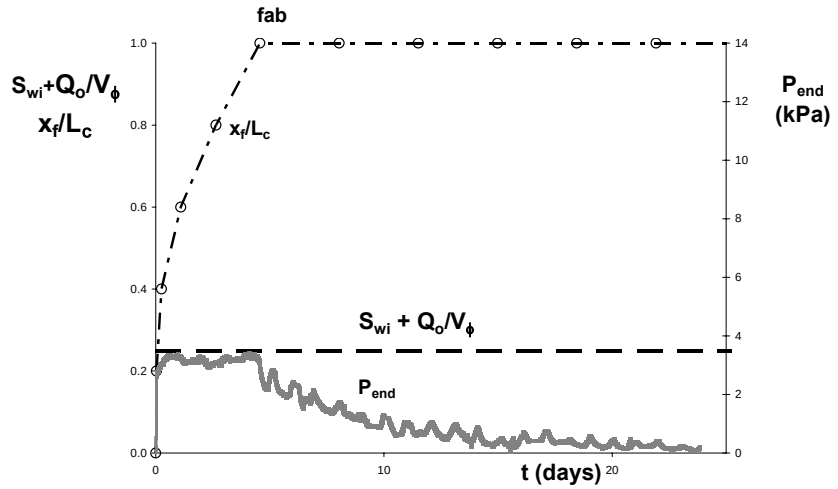

Fig. 6-6 The end pressure, distance of invasion and oil production for core HB3 (initially saturated with mineral oil, S_{wi}=25%). (HB3, VSWW,S_{wi} = 25 %)

Cores aged with crude oil with an initial water saturation. MXW

HD2, MXW,S_{wi} =16.8 %

The main core segment was saturated with 83.2% Cottonwood crude oil and 16.8% initial water saturation, and then aged at 75^{o}C for 10 days.

The end pressure rose to 2.7 *kPa* within 1.3 days after the composite core was immersed in brine and remained at about 2.8 *kPa* until the invading brine reached the dead end (4.5 days after the composite core had been immersed). Results for core HD2 are shown in Fig. 6-7. The end pressure gradually fell over 29 days to 0.3 *kPa* and then remained close to this value for 16 days.

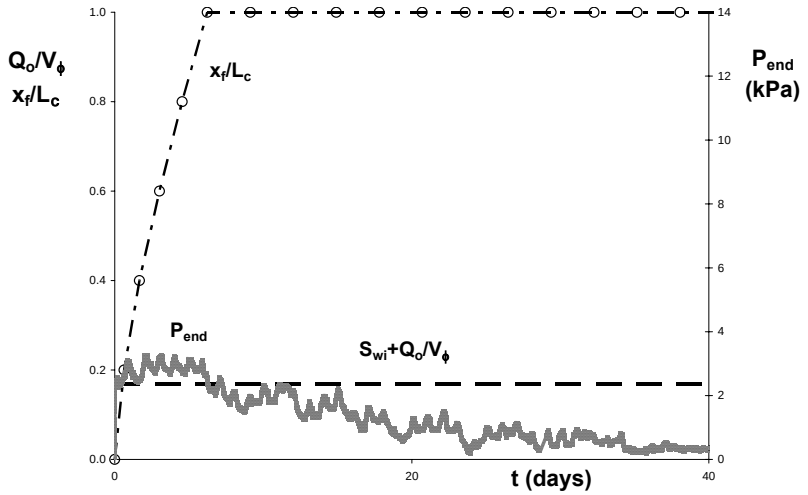

Fig. 6-7 Measurement of P_{end} (MXW) for core HD2 initially saturated with crude oil at S_{wi}=16.8% and then aged. HD2, MXW,S_{wi} =16.8 %

HO3, MXW,S_{wi} =25.3 %

The main core segment was aged at 75°C for 10 days with Cottonwood crude oil at 25.3% initial water saturation.

The end pressure rose to 5.2 *kPa* within 0.3 hours of the composite core being immersed in brine and remained at 5.6 *kPa* until the front reached the dead end (14 days after the composite core had been immersed). Results for core HO3 are shown in Fig. 6-8. The end pressure then fell. The end pressure dropped to 3.5 *kPa* 0.4 days after the front reached the dead end.

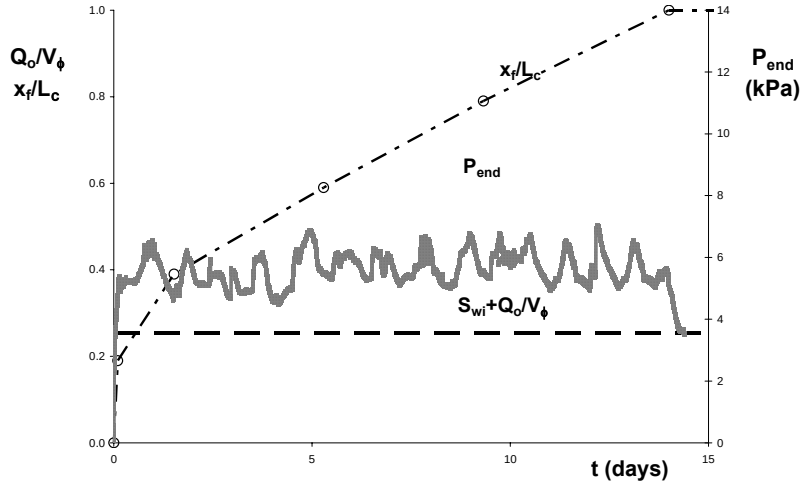

Fig. 6-8 Measurement of P_{end} (MXW) for core HO3 initially aged with crude oil at 25.3% initial water saturation.

Table 6-1

HIGH K CORE	D (cm)	L_c (cm)	K (μm^2)	ϕ (%)	Swi %	ρ_o	μ_o (Pa.s)	P_{cf} (kPa)	σ mN/m	Pcf/σ (μm^{-1})	TYPE	PROBE OIL
H6O	3.795	6.967	1.067	22.2	0	0.783	0.0038	12.40	48.85	0.254	VSWW	Mineral
HF4	3.37	3.171	0.964	22.3	0	0.783	0.0038	14.4	48.85	0.295	VSWW	Mineral
HC4	3.406	6.555	0.991	22	0	0.8874	0.2041	1.6	29.7	0.054	WWW	Crude
HE2	3.599	6.332	0.991	22	0	0.8874	0.2041	1.64	29.7	0.055	WWW	Crude
HB1	3.343	6.567	0.86	21.5	17.9	0.783	0.0038	4.70	48.85	0.096	VSWW	Mineral
HB3	3.248	6.555	1.022	22.2	25	0.783	0.0038	3.30	48.85	0.068	VSWW	Mineral
HD2	3.151	6.215	1.055	22.7	16.8	0.8874	0.0241	2.66	29.7	0.090	MXW	Crude
HO3	3.703	6.45	1.026	22	25.3	0.8874	0.0241	5.50	29.7	0.185	MXW	Crude

Task 7. *Novel imbibition measurements on mixed-wet rock and network models.*

Countercurrent spontaneous imbibition experiments on oil reservoir rocks are usually carried out using cylindrical cores of rock. Sometimes the cores are sealed on some of the faces, and experiments then give production curves of different duration and slightly different shape. Results can be correlated for rock properties such as porosity and permeability and fluid properties such as viscosity and interfacial tension. An overall or average scale factor correlates for different core sizes and shapes. Although the real imbibition process is actually quite complicated, by making the approximations that there is (a) frontal displacement and (b) constant saturation behind the front, a simple analytical solution is possible. The analysis gives a new shape scale factor. These assumptions also allow the scale factors of Ma *et al*. and Ruth *et al.* to be used to predict the shape of the production curves. Countercurrent spontaneous imbibition experiments using matched cores of different shape were carried out to challenge the Ma, Ruth and new scale factors. In particular, cylindrical cores with an axial hole were used with either the inner or outer cylindrical face open to give radial geometry with imbibition into a contracting or expanding volume. The experimental results confirmed that the Ma and Ruth scale factors are good to excellent for most situations but that the new one is marginally better for extreme shape variations. Variability between the cores caused by not having enough exposed surface and not enough rock depth seems to be of greater importance than the differences between the three scale factors.

Introduction to Novel imbibition measurements on mixed-wet rock and network models.

Countercurrent spontaneous imbibition occurs when a wetting fluid displaces a less-wetting fluid from the pore space of a porous medium. The wetting fluid imbibes into the pore space and the non-wetting fluid is expelled. In systems with one-dimensional geometry such as a cylinder open at one end and other geometries, the mass balance requirement means that the flows of the two fluids are equal but in opposite directions. Also, experimentally, in some circumstances a saturation front is observed to advance through the system. A positive pressure has to build up at the dead end of the system and it is this pressure that pushes the non-wetting phase back through the invading wetting phase (Li *et al*., 2003, 2006). Countercurrent imbibition is believed to be a mechanism by which oil can be displaced from the rock in fractured reservoirs (Morrow & Mason, 2001).

Countercurrent imbibition in reservoir rocks is usually studied at the core level using cylindrical cores about 70mm long and with a diameter of about 35 to 50mm. A typical experiment consists of saturating a core with oil and then immersing it in brine. The expelled oil is collected and its volume is measured. Results are recorded as the total amount of oil produced at various time intervals. Attempts have been made to correlate results for very strongly water wet imbibition so that the effect of changing interfacial tension, rock porosity and permeability can be predicted (Mattax & Kyte, 1962). There are two additional factors - the viscosities of the two phases and the shape of the sample. This report addresses the latter problem. Frequently cores used in experiments have all faces of the cylinder open to the invading phase. The experiments give rapid and reproducible results but the flow patterns are complex and, therefore, difficult to model. If the ends of the core cylinder are sealed then the flows become radial. The simplest case, however, reducing imbibition to a one-dimensional, linear situation, is to seal the outer surface plus one end, thus leaving one end open for the imbibition and production to take place. Because the shape of the sample makes a difference to the shape of the production *vs* time results, it would be convenient to be able to transform experimental results obtained from one core geometry into those from another (Behbahani *et al*., 2006). A function involving the core sample shape which was found to correlate available data reasonably well is (Ma *et al*. 1997):

$$t_D = \frac{1}{L_c^2}\sqrt{\frac{K}{\varphi}}\frac{\sigma}{\sqrt{\mu_w \mu_{nw}}}t \qquad (7\text{-}1)$$

where L_c is a characteristic length, K the rock permeability, φ its porosity, σ is the interfacial tension between the phases and μ_w and μ_{nw} are the viscosities of the wetting and non-wetting phases. This expression has been recently applied to cores of different shape (Yildez *et al.,* 2006)

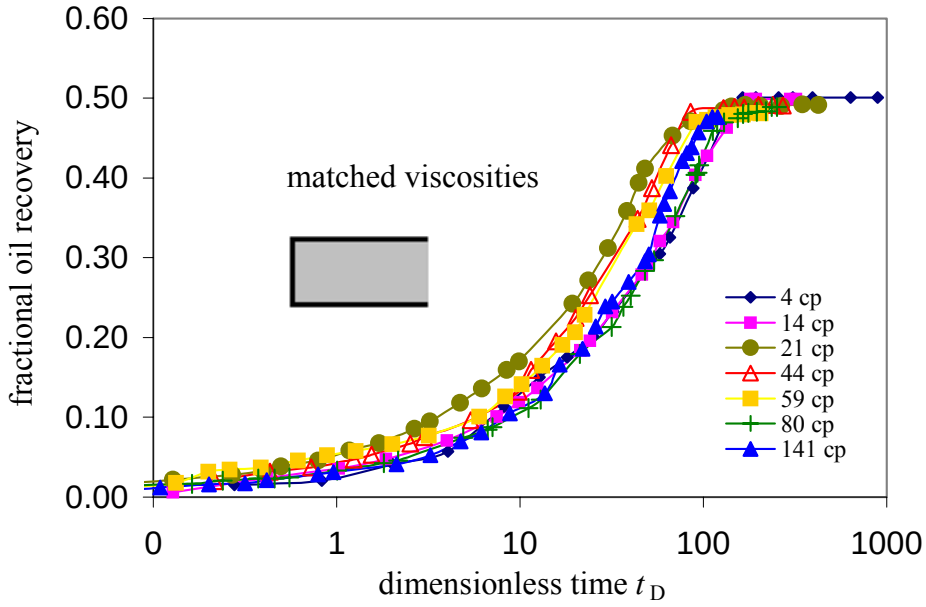

Figure 7-1. Typical experimental data correlated by Eq. (7-1). The data is taken from Fischer & Morrow, 2006, and is for linear countercurrent spontaneous imbibition into one-end-open cores with similar properties. The two fluids have matched viscosities.

Figure 7-1 shows a correlation (Fischer & Morrow, 2006) for matched viscosities and one end open. In Eq. 7-1, t_D is a normalised dimensionless time and it is obtained by multiplying the actual time (t) by a function of rock and fluid properties. Ma's semi-empirical correlation (1997) for the general characteristic length L_c is

$$L_c = \sqrt{V \Big/ \sum_{i=1}^{n} A_i / x_{A,i}} \qquad (7\text{-}2)$$

where V is the bulk volume of the matrix, A_i is the area open to imbibition in the ith direction, $x_{A,i}$ is the distance from A_i to the no-flow boundary and n is the number of faces open to imbibition. For linear imbibition L_c is simply the length of the core. For a cylindrical core with all faces open it becomes

$$L_c = \frac{L_{max} d}{2\sqrt{d^2 + 2L_{max}^2}} \qquad (7\text{-}3)$$

where L_{max} is the core length and d is the core diameter. Note that the correlation just brings the data together and on a $\log_{10}$ scale changes in the characteristic length L_c only move the production curves left and right. The characteristic length does not predict the form of the production *vs* t_D function. The function in Eq. 7-1 involves the core permeability K and porosity φ; σ is the interfacial tension and t is the actual time. L_c is a characteristic length which includes both size and shape and is given by Eq. 7-2. The interesting factor is the $\sqrt{\mu_w \mu_{nw}}$ term because it involves only the viscosities of the wetting and non-wetting phases without any explicit dependence on relative permeabilities. The correlation only involves the time axis; the other axis is usually presented as the fraction of the pore volume filled with wetting phase (i.e. the recovery), although this is sometimes normalised by division by the oil recovered at infinite time. The core shape factor which determines the characteristic length has been investigated in some detail by Ma *et al*. (1997) and later by Ruth *et al*. (2003). However, their work was mainly concerned with the general correlation of the imbibition curve's *location* on a $\log_{10} t$ scale rather than the changes in function form brought about by different sample shapes. Recent experiments (Fischer & Morrow, 2005) have demonstrated the small but systematic differences in the form of imbibition production curves particularly between the one-dimensional and all-faces-open configurations that are normally used in experiments. For co-current imbibition Zimmerman *et al*. (1990) predicted such differences in shape using both numerical simulation and an approximation method. It is the purpose of this report to indicate an *a priori* shape for the countercurrent imbibition production function and to quantify the small differences in function shape caused by different sample geometry.

Frontal Imbibition. General

In some cases one-dimensional countercurrent imbibition is primarily a frontal process because, during experiments, a liquid front can be seen to advance along the core (Li *et al.,* 2003). The volume imbibed relative to the core porosity multiplied by the distance that the front has advanced gives an indication of the step change in saturation at the front. The final amount imbibed relative to the total volume of the pore space gives an indication of the final saturation.

From these values one can conclude that about 80% of the imbibition recovery reported by Li *et al*. occurs as frontal displacement. This does not mean that all countercurrent spontaneous imbibition is a frontal process, just which in some circumstances it is.

In simulation of one-dimensional countercurrent imbibition, it has been shown (Li *et al.,* 2003) that the front and its small amount of dispersed imbibition could be represented by a self-similar front. By self-similar we mean that the saturation profile with distance is always the same provided that the distance to the front is properly scaled. The self-similar front is a consequence of the mathematical formulation of countercurrent imbibition. There are three functions, all of saturation; there is the capillary pressure, and two relative permeabilities, one for the wetting phase and the other for the non-wetting phase. The consequence is that, for a thin slice of core, if the relative permeability for one phase is fixed then there is only a single value for the relative permeability for the other phase. Added to this is the fact that, for pure countercurrent spontaneous imbibition, the flow of one phase through the slice is exactly equalled by the reverse flow of the other phase, and both these are over the same area. The concept of a single function representing capillary pressure has been recently challenged by Le Guen & Kovscek (2006) who suggest that non-equilibrium effects should be taken into account. If this behaviour obtains, it would add another variable.

As a limiting case, following Cil & Reis (1996), we could imagine that ALL of the saturation change takes place at the saturation front where the saturation makes a step change from S_{wi} (the initial wetting phase saturation) to S_{wf} (the wetting phase saturation at the front). This assumption means that the saturation behind the front is constant at S_{wf}. Behind the front therefore, the relative permeabilities of each of the two phases are also constant. Also, because there is no change in saturation behind the front, the flow of wetting phase (q_{w}) at one instant in time is invariant with distance from the open face. Up to the front, the flow of non-wetting phase (q_{nw}) is also invariant. It must be stressed that this is an approximation, but it provides a tractable model that may be approximately realistic for some cases of imbibition. Darcy's law gives the two flows:

$$q_{\mathrm{w}} = -\frac{Kk_{\mathrm{rw}}A}{\mu_{\mathrm{w}}}\frac{\partial P_{\mathrm{w}}}{\partial x} \qquad (7\text{-}4)$$

$$q_{\mathrm{nw}} = -\frac{Kk_{\mathrm{rnw}}A}{\mu_{\mathrm{nw}}}\frac{\partial P_{\mathrm{nw}}}{\partial x} \qquad (7\text{-}5)$$

where K is the permeability, k_{rw} and k_{rnw} are the relative permeabilities to the respective phases, μ_{w} and μ_{nw} are the respective viscosities, A is the area and x is a distance. The capillary pressure P_{c} is the difference between the pressure in the non-wetting phase (P_{nw}) and the pressure in the wetting phase (P_{w}).

$$P_{\mathrm{c}} = P_{\mathrm{nw}} - P_{\mathrm{w}} \qquad (7\text{-}6)$$

and flow continuity gives:

$$q_{\mathrm{w}} = -q_{\mathrm{nw}} \tag{7-7}$$

Combining equations 7-6 to 7-7 gives:

$$q_{\mathrm{w}} = \frac{Kk_{\mathrm{rw}}k_{\mathrm{rnw}}A}{\mu_{\mathrm{w}}k_{\mathrm{rnw}} + \mu_{\mathrm{nw}}k_{\mathrm{rw}}}\frac{\partial P_{\mathrm{c}}}{\partial x} \tag{7-8}$$

Because the saturation has been assumed to be constant behind the front, a large part of this equation will be constant. Let M be a mobility factor and let

$$M = \frac{k_{\mathrm{rw}}k_{\mathrm{rnw}}}{\mu_{\mathrm{w}}k_{\mathrm{rnw}} + \mu_{\mathrm{nw}}k_{\mathrm{rw}}} \tag{7-9}$$

For constant saturation the relative permeabilities have to be constant, consequently the factor M will be constant and so, behind the front

$$q_{\mathrm{w}} = KMA\frac{\partial P_{\mathrm{c}}}{\partial x} \tag{7-10}$$

It should be noted that for the assumption that the saturation behind the front is constant to be approximately true, P_{c} has to be able to vary a lot (so as to be able to drive the flows) for negligible changes in S_{w} (i.e. the gradient of the capillary pressure curve with saturation is steep).

Because the mobility factor M is constant for the flows behind the wetting front, Eq. 7-10 can be integrated between the open face of the core and the front. For one-dimensional imbibition the area A will be a constant. However, for radial flows into a cylinder with capped ends, the area A will vary with the distance and so the function for the amount of imbibition versus time will be different. It is the effect of the change in areas with distance and its effect on the overall resistance to flow and the changes it makes to the rate of frontal advance that are the main factors in the following analysis.

The flow of wetting phase arriving at the front advances the position of the front. A mass balance gives

$$\frac{\mathrm{d}x_{\mathrm{f}}}{\mathrm{d}t} = \frac{q_{\mathrm{w}}}{\varphi A\left(S_{\mathrm{wf}} - S_{\mathrm{wi}}\right)} \tag{7-11}$$

where x_{f} is the distance of the front from the open face. S_{wi} is the initial saturation and S_{wf} is the saturation behind the front.

One Dimensional Countercurrent Imbibition

The experimental situation is of a core initially mostly filled with non-wetting phase and sealed on all faces except one end. Starting with Washburn (1921), for co-current imbibition this case

has been investigated many times. It gives the base case with which other core shapes can be compared.

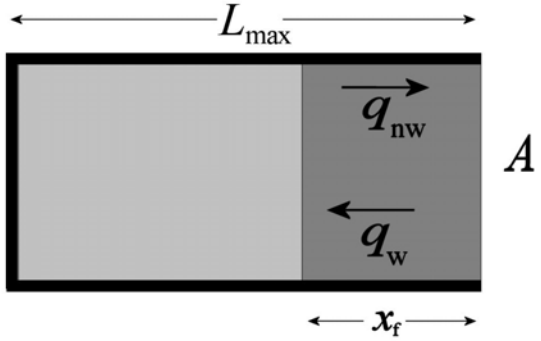

Figure 7-2. Diagram showing linear countercurrent imbibition.

In Eq. 7-10 q_w, M and A do not vary with x and so the equation can be integrated between the open face and the front to give:

$$q_w(x_f - 0) = KMA(P_{cf} - P_{co}) \qquad (7\text{-}12)$$

P_{cf} is the capillary pressure difference at the front. P_{co} is the capillary pressure difference at the open face. At the open face the pressure in the wetting phase is zero but the pressure in the non-wetting phase is not zero It is not zero because non-wetting phase has to be bubbled from the rock into the wetting phase (Li *et al*., 2006). Substituting for q_w using Eq. 7-12 in Eq. 7-11 and integrating between the open face and the distance of the front, x_f, gives:

$$x_f^2 = \frac{2KM(P_{cf} - P_{co})}{\varphi(S_{wf} - S_{wi})}t \qquad (7\text{-}13)$$

The time t is zero when the front is at the open face. If f is the fractional amount of non-wetting phase produced at time t, then, for core length L_{max}, $f = x_f / L_{max}$ and

$$f^2 = \frac{2}{L_{max}^2}\frac{KM(P_{cf} - P_{co})}{\varphi(S_{wf} - S_{wi})}t \qquad (7\text{-}14)$$

For cylindrical tubes the capillary pressure is related to mean pore radius r_{mean} by

$$P_c = \frac{2\sigma}{r_{mean}} \qquad (7\text{-}15)$$

and, again for a bundle of cylindrical tubes, the tube radius is related to the permeability and porosity by (Pirson 1958)

$$r_{mean} = \sqrt{\frac{8K}{\varphi}} \qquad (7\text{-}16)$$

Equation 7-12 contains a difference in capillary pressures $(P_{cf} - P_{co})$. The capillary pressure at the front (P_{cf}) is mainly produced by the smaller pores and the capillary pressure at the open face (P_{co}) is mainly produced by the larger pores. The difference between them is thus related to the spread of the pore size distribution. For a spread of pore sizes, $(P_{cf} - P_{co})$ can be related to the mean capillary pressure, P_c, by a factor C_{spread} which is in some way determined by the breadth and shape of the pore size distribution. Just how does not concern us at the moment. Thus

$$P_{cf} - P_{co} = C_{spread} P_c = C_{spread} \frac{2\sigma}{r_{mean}} = C_{spread} 2\sigma \sqrt{\frac{\varphi}{8K}} \qquad (7\text{-}17)$$

Eliminating $(P_{cf} - P_{co})$ from Eq. 7-14 gives

$$f^2 = \frac{1}{L_{max}^2} \sqrt{\frac{2K}{\varphi}} \frac{MC_{spread}\sigma}{(S_{wf} - S_{wi})} t \qquad (7\text{-}18)$$

Comparison of Eq 7-18 with the correlation of Eq. 7-1 shows close similarity. The spread in pore size distributions may well make C_{spread} constant for related rock types (Berea sandstone, for example). The major difference between the two is the way in which the viscosities of the two phases enter the functions. In Eq. 7-1 it is as the geometric mean and in Eq. 7-18 it is in the mobility factor M as a combination of relative permabilities and viscosities plus the effect of C_{spread}. Quite why the relative permeabilities would relate in this way with viscosities is still a question to be answered. In Eq. 7-1 the functional form of the fraction filled is unknown whereas in Eq. 7-18 it is simply a squared term. Eq. 7-18 can be rearranged so as to be explicit for t:

$$t_{f,Linear} = \sqrt{\frac{\varphi}{2K}} \frac{(S_{wf} - S_{wi})}{MC_{spread}\sigma} L_{max}^2 f^2 \qquad (7\text{-}19)$$

This equation now predicts the time for fractional production f from a core of length L_{max} for linear imbibition. When experiments are carried out both the time and fractional production are determined. Thus the shape of the experimental production curve can be compared to the theoretical prediction. The time for the front to reach the end of the core, t_{end}, when imbibition ceases will be

$$t_{end} = L_{max}^2 \sqrt{\frac{\varphi}{2K}} \frac{(S_{wf} - S_{wi})}{MC_{spread}\sigma} \qquad (7\text{-}20)$$

This equation is in exact agreement with Ma's equation which gives the characteristic length for this geometry L_c as the length of the core L_{max}. Note, however, that Eq. 7-19 predicts the actual shape of the production curve.

Radial Countercurrent Imbibition

Radial inwards

For radial inwards imbibition the core sample is a cylinder with a central cylindrical hole (which may or may not be present), radius R_{closed}, and with both ends and the surface of the inner hole sealed. Imbibition is radial inwards towards the core axis from the outside of the cylinder. At a time *t* the front has reached a position R_f (measured from the core axis) from its starting position at R_{open}, the core radius, at $t = 0$ (see Fig. 7-3). Again, by assuming that the core has a constant saturation behind the front, S_{wf}, the total radial flow inwards does not vary with distance behind the front.

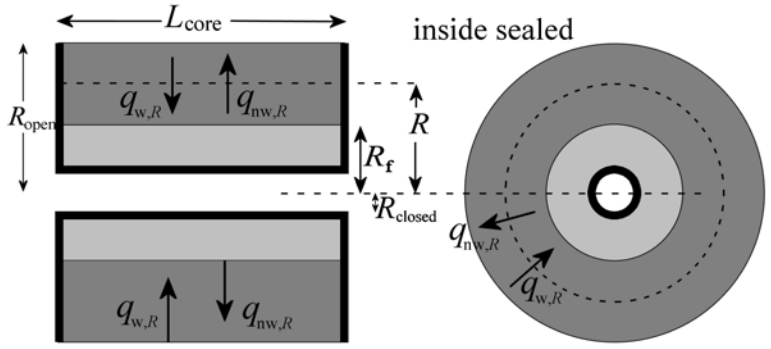

Figure 7-3. Diagram of dimensions in radial imbibition. There is a sealed hole in the center of the core so that imbibition takes place from the outside moving in. The total radial flow is constant everywhere behind the front. Compared to linear imbibition, proportionally more of the core is near the open face.

For some general intermediate position, *R*, between the front and the outside of the core Eq. 7-10 applies

$$q_{w,R} = KMA_R \frac{\partial P_c}{\partial x} \qquad (7\text{-}21)$$

Unlike the linear case the area, A_R, is now a function of *R*. If the core length is L_{core} then the area A_R becomes $2\pi RL_{core}$ and ∂x becomes $-\partial R$. Hence

$$q_{w,R} = -KM\,2\pi RL_{core} \frac{\partial P_c}{\partial R} \qquad (7\text{-}22)$$

As before $q_{w,R}$ is invariant (with *R*) and so Eq. 7-22 can be integrated to give

$$\ln \frac{R_f}{R_{open}} = -\frac{KM\,2\pi L_{core}\left(P_{cf} - P_{co}\right)}{q_{w,R}} \qquad (7\text{-}23)$$

Again Eq. 7-11 gives the distance advanced by the front (-dR_f) in time d*t* in terms of $q_{w,R}$

$$\frac{dR_f}{dt} = -\frac{q_{w,R}}{2\pi R_f L_{core}\varphi\left(S_{wf} - S_{wi}\right)} \qquad (7\text{-}24)$$

except that now the area which was previously constant is now A_R, and is a function of R_f. Eliminating $q_{w,R}$ between Eq. 7-23 and Eq. 7-24 gives

$$\frac{R_f}{R_{open}} \ln \frac{R_f}{R_{open}} d\left(\frac{R_f}{R_{open}}\right) = \frac{1}{R_{open}^2} \frac{KM(P_{cf} - P_{co})}{\varphi(S_{wf} - S_{wi})} dt \quad (7\text{-}25)$$

Integration of Eq. (7.25) from $t = 0, R_f = R_{open}$ to (t, R_f) gives

$$1 + 2\left(\frac{R_f}{R_{open}}\right)^2 \ln \frac{R_f}{R_{open}} - \left(\frac{R_f}{R_{open}}\right)^2 = \frac{4}{R_{open}^2} \frac{KM(P_{cf} - P_{co})}{\varphi(S_{wf} - S_{wi})} t \quad (7\text{-}26)$$

Replacing the P_c's with K, φ, and C_{spread} as before using Eq. 7-17 gives,

$$1 + 2\left(\frac{R_f}{R_{open}}\right)^2 \ln \frac{R_f}{R_{open}} - \left(\frac{R_f}{R_{open}}\right)^2 = \frac{2}{R_{open}^2} \sqrt{\frac{2K}{\varphi}} \frac{C_{spread} M\sigma}{(S_{wf} - S_{wi})} t \quad (7\text{-}27)$$

The fraction of the total imbibition when the front is at R_f is

$$f = \frac{R_{open}^2 - R_f^2}{R_{open}^2 - R_{closed}^2} \quad (7\text{-}28)$$

giving

$$\left(\frac{R_f}{R_{open}}\right)^2 = 1 - f\left(1 - \left(\frac{R_{closed}}{R_{open}}\right)^2\right) \quad (7\text{-}29)$$

Thus

$$f - f\left(\frac{R_{closed}}{R_{open}}\right)^2 + \left(1 - f + f\left(\frac{R_{closed}}{R_{open}}\right)^2\right) \ln\left(1 - f + f\left(\frac{R_{closed}}{R_{open}}\right)^2\right) = \frac{2}{R_{open}^2} \sqrt{\frac{2K}{\varphi}} \frac{MC_{spread}\sigma}{(S_{wf} - S_{wi})} t \quad (7\text{-}30)$$

The time taken for the front to reach the centre of the core $(R_f = R_{closed})$ when imbibition stops, t_{end}, is

$$t_{end} = \frac{1}{2}\left(R_{open}^2 + 2R_{closed}^2 \ln \frac{R_{closed}}{R_{open}} - R_{closed}^2\right) \sqrt{\frac{\varphi}{2K}} \frac{(S_{wf} - S_{wi})}{MC_{spread}\sigma} \quad (7\text{-}31)$$

The characteristic length given by Ma's equation for a solid cylinder of infinite length is $L_c = R_{max} / \sqrt{2}$ and Eq. 7-31 agrees exactly with it when $R_{closed} = 0$. However, when the core has an inner circular hole, Ma's method for calculating the characteristic length (Ma *et al.*, 1997) gives

$$L_{c,Ma}^2 = \frac{\left(R_{open} - R_{closed}\right)^2}{2}\left(1 + \frac{R_{closed}}{R_{open}}\right) \qquad (7\text{-}32)$$

Ruth *et al.*(2003*)* improved on this factor by compensating for situations where incremental volumes of the sample do not have the same sizes at different distances from the open face. If the Ruth factor is scaled relative to the Ruth linear function and is factorised one obtains

$$L_{c,Ruth}^2 = \frac{\left(R_{open} - R_{closed}\right)^2}{3}\left(1 + 2\frac{R_{closed}}{R_{open}}\right) \qquad (7\text{-}33)$$

Eq. 7-31 here not only compensates for incremental volumes being at different distances (like Ruth's) but also compensates for the variation in resistance with distance between the incremental volume and the open face and gives:

$$L_c^2 = \frac{1}{2}\left(R_{open}^2 + 2R_{closed}^2 \ln\frac{R_{closed}}{R_{open}} - R_{closed}^2\right) \qquad (7\text{-}34)$$

Note that all three scale factors agree when R_{closed} is almost equal to R_{open} and L_c equals $R_{open} - R_{closed}$. This is not surprising because the geometry is a thin laminar sheet in which imbibition is linear in theory and there are no effects of the radial geometry.

Radial outwards

The radial outwards situation is shown in Fig. 4. The equation governing flow is the same as Eq. 7-23 because of the way R_{closed} and R_{open} have been defined.

$$\ln\frac{R_f}{R_{closed}} = -\frac{KM\,2\pi L_{core}\left(P_{cf} - P_{co}\right)}{q_{w,R}} \qquad (7\text{-}35)$$

The analysis is as before with $q_{w,R}$ being invariant with R. Its elimination, followed by integration from $t = 0$, $R_f = R_{open}$ to $\left(t, R_{closed}\right)$ and replacement of the P_c's with K, φ, and C_{spread}, gives exactly the same equation as Eq. 7-27. Even the equation for the fraction of imbibition, *f*, is unchanged. It follows that the equation for the time taken for the front to reach the closed boundary, t_{end}, is also unchanged as is the scale factor, L_c^2. Numerically the times and scale factors between radial inwards and radial outwards imbibition will differ because R_{open} and R_{closed} are different. The basic equations, however, are the same.

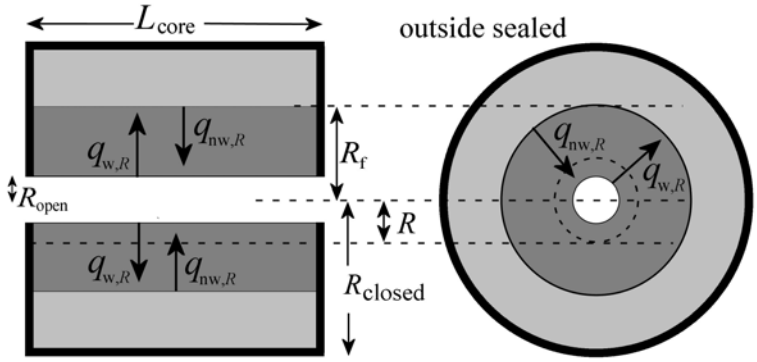

Figure 7-4. Diagram showing the variables for a cylindrical core sealed on the outside with countercurrent imbibition occurring from a cylindrical central hole. Compared to linear imbibition, proportionally more of the core is further from the open face.

Radial scale factors

Equations 7-32, 7-33, and 7-34 give the scale factors for the Ma, Ruth and the current analysis (now termed Mason, for short). They are all slightly different and only agree when the hole is virtually the same diameter as the core when imbibition becomes essentially linear. For the radial inwards situation a comparison of the various functions can be made in different ways. Figure 7-5 shows the scale factors plotted against the aspect ratio of the hole in the cylinder and with a cylinder diameter of unity. Considering their different functional form, the Ma and Mason functions are surprisingly close.

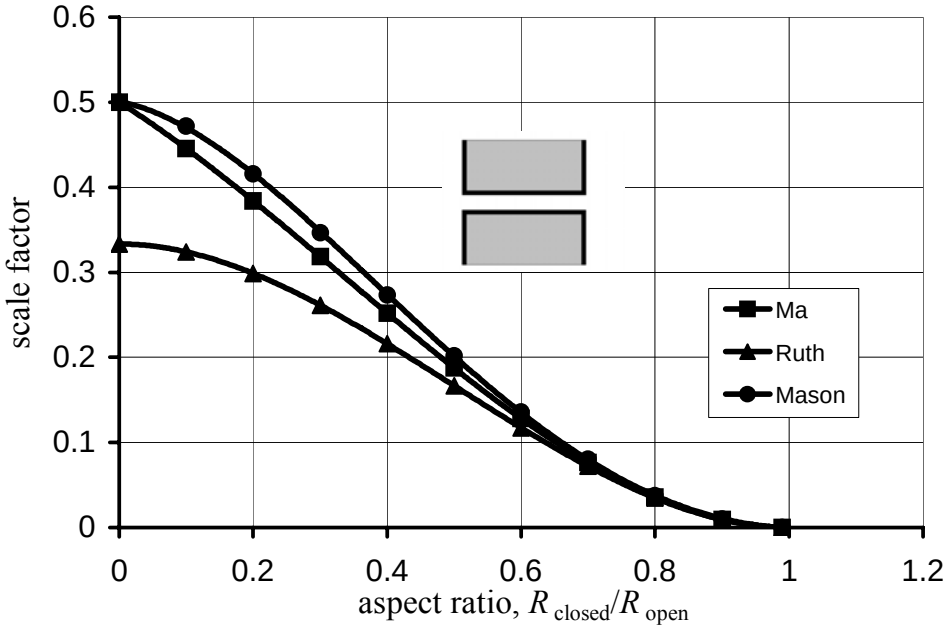

Figure 7-5. Comparison of the scale factors calculated using the Ma, Ruth and present (Mason) functions for radial-inwards imbibition. Note that all three start at the same values when R_{closed} is almost equal to R_{open} which approximates to the linear situation.

All of the lines on Fig. 7-5 run approximately from (0, 0.5) to (1, 0) and this suggests a better way of normalising the functions. Division by $(R_{\text{open}} - R_{\text{closed}})^2$ is normalising with respect to the square of the distance from the open face to the no-flow boundary. Figure 7-6 shows the same scale factors plotted in this normalised way. Linear imbibition scaled in the same way has a normalised scale factor of unity.

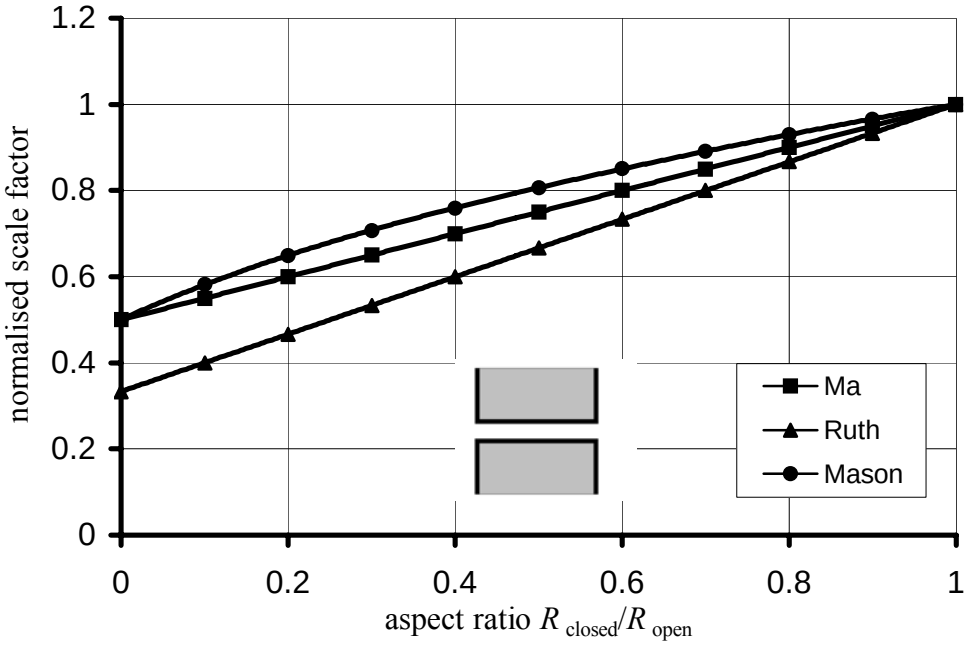

Figure 7-6. The normalised scale factor is obtained by dividing the scale factor by the square of the distance from the open boundary to the closed boundary. This normalised factor is almost linear for all three functions.

Comparison with linear imbibition with the same penetration distance ($L_{\max}$ in one case, $\left(R_{\text{open}} - R_{\text{closed}}\right)$ in the other) shows that radial inward imbibition is always proportionally faster and, for the solid cylinder and the Ma and Mason functions, takes half of the time. There are two reasons. One is that there is less volume swept and the other is that proportionally more of the core is nearer the open face in the radial situation. The volume to be filled tends to zero as the axis of the core is approached by the front whereas in linear imbibition there is constant pore volume with position as the front approaches the end of the core.

For the radial outwards situation the scale factors become infinite as the radius of the hole in the center of the core goes to zero. Consequently we restrict ourselves to practical ratios. Normalised scale factors for radial outwards imbibition are shown in Fig. 7-7. It can be seen from Fig. 7-7 that the three scale factors begin to differ significantly once the aspect ratio ($R_{\text{closed}}/\text{R}_{\text{open}}$) goes much above 2.

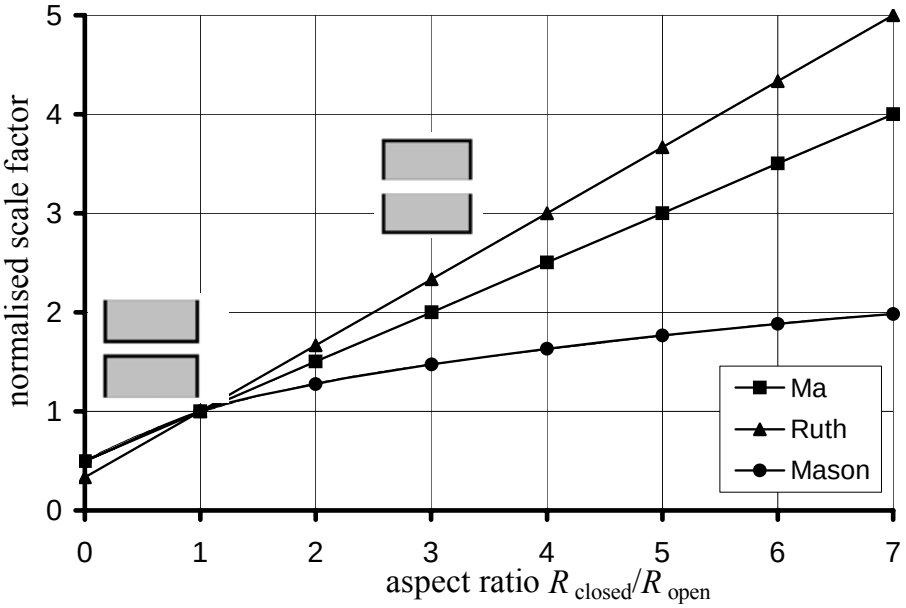

Figure 7-7. Radial imbition outwards is where the aspect ratio is greater than unity. Because the normalised scale factors are always above 1 for radial outwards imbibition, imbibition in such a geometry is proportionally much slower than for the linear situation (for which the normalised scale factor is 1)

Fractional production

The key assumption has been that frontal imbibition takes place. There is a further consequence of this assumption: imbibition ceases suddenly when the front reaches the closed boundary at the time t_{end}. With cylindrical geometry it was t_{end} that determined the scale factor. Because the front position does not depend on the closed boundary until it actually reaches it, it follows that the shape of the production curve is independent of the actual boundary location. The scale factor (L_c) is determined by the final front position (i.e. the closed boundary) as well as the core shape. The scale factor is thus the ultimate consequence of the production curve. For radial imbibition and a fractional production of *f*, the value of R_f is given by Eqn(7-28), or explicitly

$$R_f^2 = R_{open}^2 - f\left(R_{open}^2 - R_{closed}^2\right) \qquad (7\text{-}36)$$

Substitution of R_f into Eq. 7-27, also 7-37 enables the appropriate time for that fractional production, *f*, to be found.

$$t_{f,\text{Mason}} = \frac{1}{2}\sqrt{\frac{\varphi}{2K}}\frac{\left(S_{wf} - S_{wi}\right)}{C_{spread} M\sigma}\left(R_{open}^2 + 2R_f^2 \ln\frac{R_f}{R_{open}} - R_f^2\right) \qquad (7\text{-}37)$$

Different core geometries produce different shaped production curves. For example, Eq. 7-19 predicts the production versus time function for linear imbibition. The combination of Eq. 7-36 and Eq. 7-37 does the same for radial imbibiton. The two are compared on Fig. 7-8 using the conventional $\log_{10} t$ on the *x*-axis. Although one is displaced relative to the other, the actual shapes look very similar when plotted in this way.

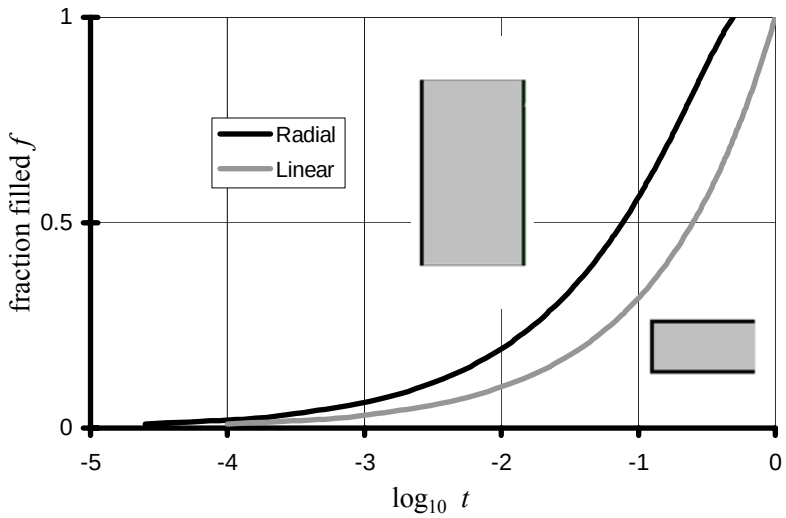

Figure 7-8. Comparison of linear and radial inwards imbibition. The fraction imbibed is plotted versus $\log_{10} t$. The length of the core in linear imbibition and the radius of the core in radial imbibition have been set to unity so that the distance the front has to travel is the same in both geometries. The factor $\sqrt{\frac{2K}{\phi}}\frac{MC_{\text{spread}}}{(S_{\text{wf}}-S_{\text{wi}})}$ has also been set at 1. No adjustment for the different characteristic lengths has been made and so the time when imbibition is completed (t_{end}) for radial imbibition is half that for linear imbibition.

In order to better emphasise the difference in shape between radial and linear imbibition production curves it is better to use a $\sqrt{time}$ axis and to normalise with respect to t_{end}. The comparison is shown in Fig. 7-9.

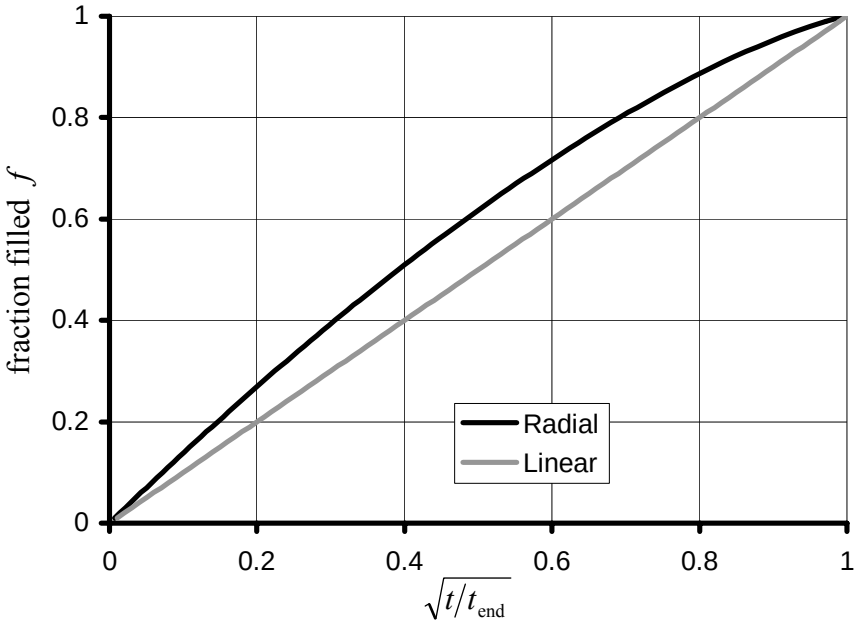

Figure 7-9. The imbibition curves of Fig. 8 plotted against the square root of normalised time $\sqrt{t/t_{end}}$. This plot clearly shows shows the effect of differences in shape. However, the two production curves are still very similar.

A similar analysis can be followed using the Ma and Ruth scale factors to predict the entire production curve. For radial imbibition the idea can be extended to cover different aspect ratio cores and with imbibition radial inwards or radial outwards and for all three functions (Ma, Ruth, Mason). There are clearly a large number of possible comparisons. However, it is known from past experiments that the shapes of countercurrent imbibition production curves are similar, especially when plotted on the usual $\log_{10} t$ scale. This can be seen from Fig. 7-8. In fact, although they look very different mathematically, the three functions (Ma, Ruth, Mason) give very similar production curves for most practical situations. To show differences one needs to go to unusual core geometries. One such is a core with a central cylindrical hole with a diameter of 0.2 times the core diameter. If sealed on the inside and both ends, this geometry gives radial inwards imbibition with an aspect ratio (R_{closed}/R_{open}) of 0.2. If sealed on the outside and both ends, the geometry is radial outwards with an aspect ratio of 5. For the same distance travelled by the front, radial inwards imbibition goes faster than linear imbibition and radial outwards imbibition goes slower. Normalising by the time imbibition is completed, t_{end}, allows comparison of the shapes of the different production curves. Also by plotting the fraction imbibed versus $\sqrt{t/t_{end}}$ makes the linear imbibition production curve a straight line. Figure 7-10 shows the production curves for a core with a central hole 0.2 times the core diameter for radial inwards, radial outwards and linear imbibition. All three functions agree fairly closely but the Mason function is closest to the two outer limits of the other functions.

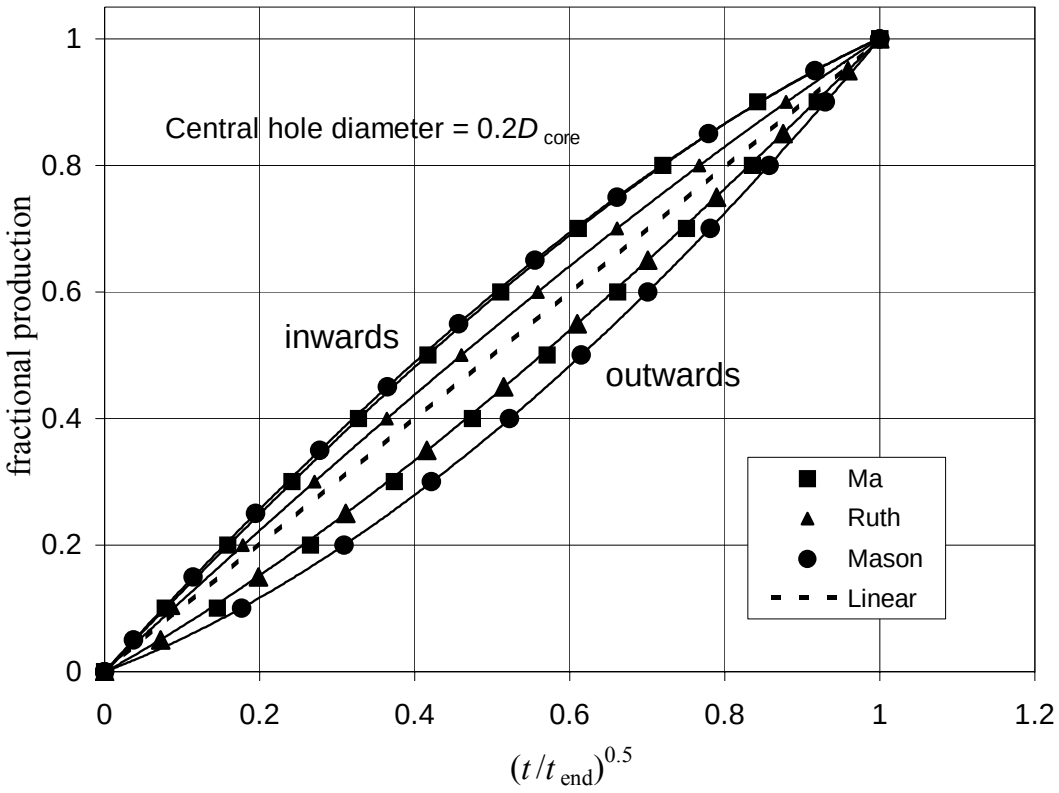

Figure 7-10. Comparison of the three functions for radial inwards, aspect ratio 0.2 (the three left hand curves) and radial outwards, aspect ratio 5 (the three right hand curves) for a core with an axial hole diameter of 0.2 times the outer core diameter. Note that all of the curves are similar and, when plotted in this way, are almost linear. For inwards imbibition the Ma and Mason functions are almost coincident. For outwards imbibition the Ma and Ruth functions are almost coincident.

Two important imbibition geometries, linear and radial inwards into a solid core, have frequently been tested by experiment. It has been observed (Fischer *et al.* 2006) that logarithmic plots of the distance of frontal advance calculated from the fraction imbibed (x_f for linear and $\left(R_{open} - R_f\right)$ for radial) *versus* time on log-log plots are straight lines. Figure 7-11 shows such plots for the three shape factors. For linear imbibition the plot is a straight line. It is also almost a straight line for the Ma, Ruth and Mason functions. However, extrapolating the straight line to full invasion saturation does not give quite the same time value as the linear case because all three curves have a small highly curved portion near to complete invasion.

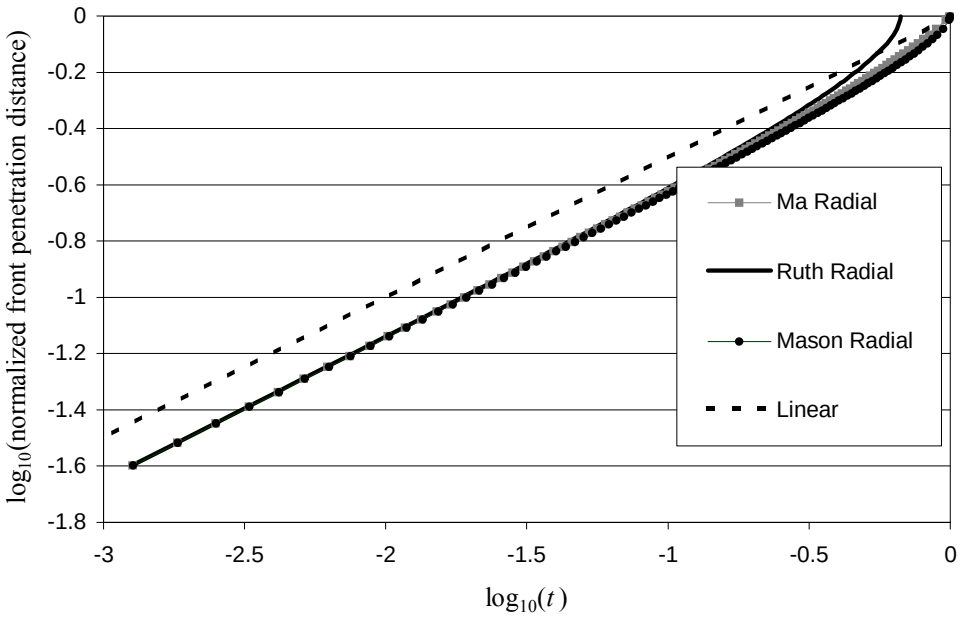

Figure 7-11 Log-log plots of the front position calculated from the fraction imbibed, *f*, for radial and linear imbibition. Note that the plots for radial imbibition are very close to being straight lines but, because of the curved parts at higher saturation, the time at which the extrapolated straight lines reach the maximum front penetration distance is longer than for the curves given by the shape factors.

A fairly simple geometry for which experiments can be readily performed is a cylindrical core with a central axial hole and with both flat ends sealed. Such a geometry exhibits simultaneous outward imbibition from the central hole and inwards imbibition from the outer surface. It is difficult to predict the scale factors using the Ma and Ruth methods because the position of the no-flow boundary is not obvious. However, the concept of frontal imbibition indicates that at the end of imbibition the no-flow boundary will be located at a radius which makes the two scale factors (one inward, one outward) the same. The end point and associated no-flow boundary are connected by the same scale factor. If R_{nf} is the radius at this no-flow boundary then, at the end of imbibition, R_{nf} is the same for the radial inwards front and the radial outwards front. If R_{outer} and R_{inner} are the two core boundary radii then, for the Ma function, Eq. 7-32 gives

$$L_{\mathrm{c,Ma}}^2 = \frac{\left(R_{\mathrm{outer}} - R_{\mathrm{nf}}\right)^2}{2}\left(1 + \frac{R_{\mathrm{nf}}}{R_{\mathrm{outer}}}\right) = \frac{\left(R_{\mathrm{inner}} - R_{\mathrm{nf}}\right)^2}{2}\left(1 + \frac{R_{\mathrm{nf}}}{R_{\mathrm{inner}}}\right) \qquad (7\text{-}38)$$

A similar equation can be written for the Ruth function, Eq. 7-33 and for the Mason function, Eq. 7-34. The Ma and Ruth functions both give cubics for R_{nf} but the Mason function gives an analytic expression for the final position of the no-flow boundary

$$R_{\mathrm{nf}}^2 = \frac{\left(R_{\mathrm{outer}}^2 - R_{\mathrm{inner}}^2\right)}{\ln\left(\frac{R_{\mathrm{outer}}^2}{R_{\mathrm{inner}}^2}\right)} \qquad (7\text{-}39)$$

If imbibition is not complete then the fronts are at two different positions. No analytic solution for the positions of the two fronts is possible and numerical solutions are required.

Experimental

Countercurrent spontaneous imbibition experiments were carried out on a series of cylindrical matched Berea Cx sandstone cores which had been cut to have different diameter holes in the center and which had different faces sealed with epoxy resin so that imbibition would be linear, radial inwards or radial outwards. The aims were to find out if any differences in the shapes of the production versus time curves could be detected and how the scale factor, L_c^2, varied with the dimensions. This rock is characterised by a very narrow air permeability range close to 70 md. Because of the unusual core shapes the relevant permeability of every core was not measured.

TABLE 7-1. CORE PROPERTIES

Linear –One End Open

Core No.	Length (cm)	Outer dia (cm)	Inner dia (cm)	Aspect ratio	Initial volume oil (mL)	Porosity	Permeability (mD)
C4-9	6.50	5.13	0	0	21.99	0.163	
C4-8	6.62	5.13	0	0	23.59	0.172	
C4-12	6.47	5.13	1.03	0.204	20.20	0.157	
C-1	5.90	5.07	2.23	0.440	15.37	0.160	
C1-25	5.97	5.07	3.01	0.593	12.48	0.159	71.50
C1-24	5.72	5.07	4.16	0.821	5.55	0.148	59.71
C1-25	5.93	5.07	4.15	0.818	5.47	0.138	

Linear –Both Ends Open

Core No.	Length (cm)	Outer dia (cm)	Inner dia (cm)	Aspect ratio	Initial volume oil (mL)	Porosity	Permeability (mD)
C4-5	6.50	5.13	0	0	22.45	0.167	
C1-25	6.32	3.48	0	0	9.50	0.158	
C4-11A	6.58	5.13	1.03	0.201	21.23	0.163	
C-5	5.88	5.06	2.22	0.439	15.67	0.164	
C4-4	6.55	5.13	2.19	0.427	16.44	0.148	
C-7	5.92	5.07	3.02	0.595	12.69	0.164	
C4-6	6.10	5.12	3.01	0.588	12.90	0.157	
C1-26	5.99	5.06	4.15	0.819	6.27	0.157	67.83
C-9	6.13	5.07	4.15	0.818	6.03	0.147	

Radial Inwards

Core No.	Length (cm)	Outer dia (cm)	Inner dia (cm)	Aspect ratio	Initial volume oil (mL)	Porosity	Permeability (mD)
C4-10	6.57	5.13	0	0	23.10	0.170	
C4-11	6.50	5.13	1.02	0.199	21.86	0.169	
C-8	5.88	5.06	2.23	0.440	16.13	0.169	
C4-14	6.15	5.13	3.00	0.585	13.61	0.163	
C1-28	5.88	5.07	4.14	0.816	6.52	0.164	70.80

Radial Outwards

Core No.	Length (cm)	Outer dia (cm)	Inner dia (cm)	Aspect ratio	Initial volume oil (mL)	Porosity	Permeability (mD)
C4-13A	6.53	5.14	1.02	5.04	21.38	0.165	
C4-1	6.41	5.13	2.25	2.28	17.53	0.163	
C1-21	6.20	5.07	3.02	1.68	13.16	0.162	72.19
C1-22	5.71	5.07	4.16	1.22	6.36	0.167	69.70

Radial Inwards and Outwards

Core No.	Length (cm)	Outer dia (cm)	Inner dia (cm)	Aspect ratio	Initial volume oil (mL)	Porosity	Permeability (mD)
C4-10	6.57	5.13	0	0	23.10	0.170	
C4-13	6.56	5.13	1.01	0.2	22.84	0.175	
C-2	6.09	5.06	2.22	0.44	16.75	0.169	
C-11	5.73	5.07	3.01	0.59	12.89	0.173	
C1-19	6.22	5.07	4.13	0.81	7.45	0.176	69.88

After the cores were cut, they were dried, evacuated and filled with oil. Their porosity was calculated from the weight difference between the empty and oil-filled states. Oil recovery versus time was measured in standard glass imbibition cells at ambient temperature. The oil was Soltrol 220 and had a viscosity of 3.996 cp. The invading phase was brine with a viscosity of 1.147 cp. The interfacial tension was 45.2 dynes/cm. Linear imbibition was conducted with cores filled with oil and sealed on all faces except one end. The data is shown in Figure 7-12. Different maximum volumes of brine are imbibed because some cores had large holes in them. Also the cores did not have identical length.

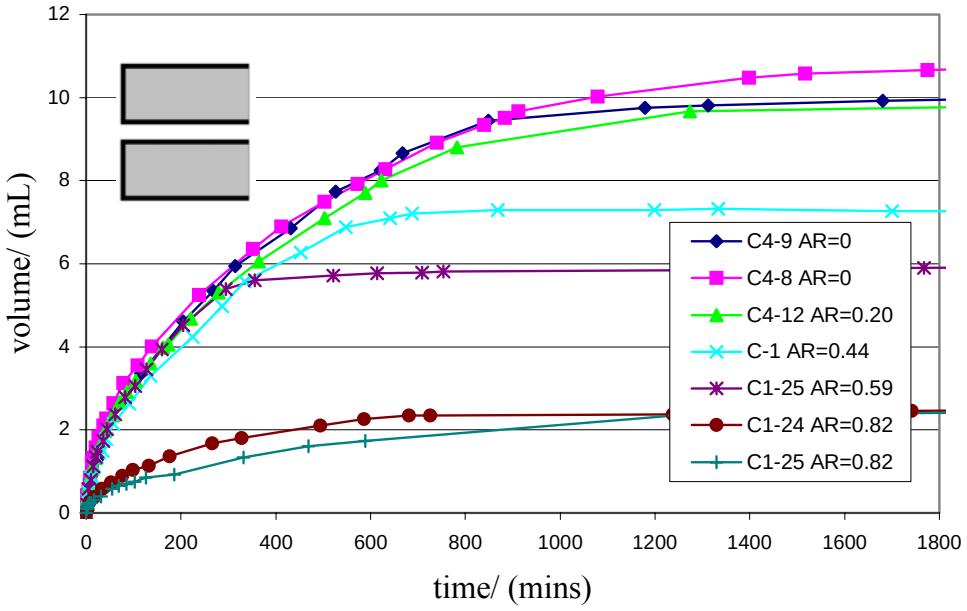

Figure 7-12. Imbibition volume *vs* time results for linear (one-end-open) countercurrent imbibition into cylindrical cores with axial holes. The cores have different pore volumes because they have holes in the middle and are of slightly different lengths.

Similar experiments were performed on cores sealed on the inside and outside but with both ends open. Imbibition thus took place from both ends simultaneously. The results are shown in Fig. 7-13,

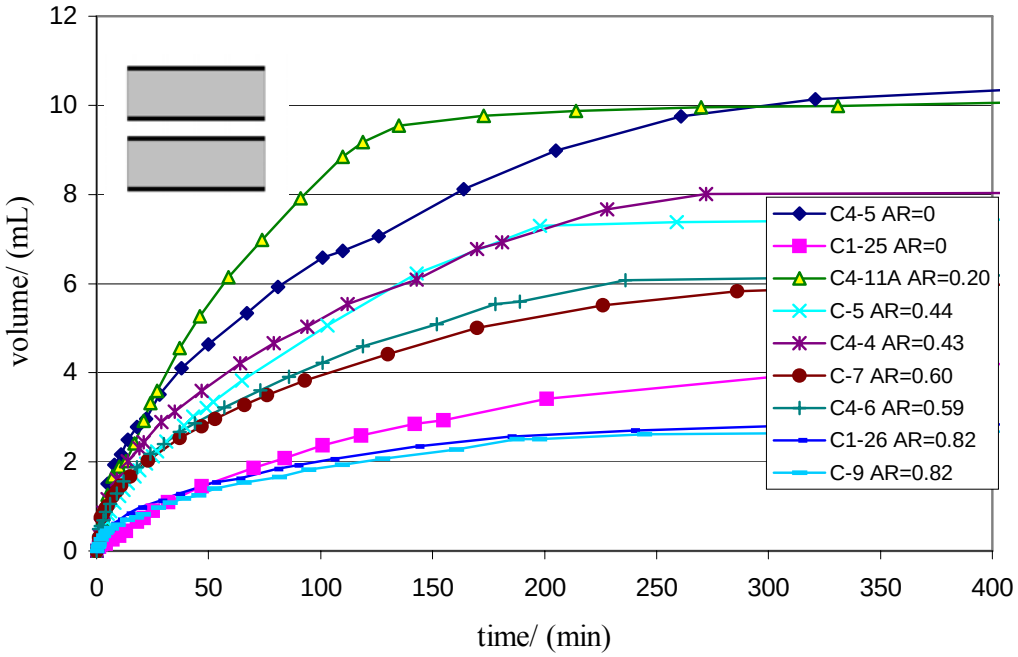

Figure 7-13. Imbibition volume versus time for linear imbibition into cores with both ends open. Note that imbibition is much faster than with only one end open (compare with Fig. 7-12).

There were three radial boundary conditions. If the only face left open is the outer one then imbibition is radial inwards. If the inner face is the only face open then imbibition is radial outwards. If both faces are open there is combined inwards and outwards radial imbibition. Results for radial inwards are shown in Figure 7-14. If there is frontal imbibition and the core properties were identical then the initial production curves for radial inwards imbibition should all fall on the same curve. This is because all of the cores have almost the same open face dimension and the position of the closed boundary cannot affect the front until the front reaches it. It can be seen that the production curves do all start together, although when the aspect ratio is 0.82 the production curve soon starts to fall off.

Results for radial outwards imbibition are shown in Figure 7-15. Because the cores all had the same outer diameter but had different diameter holes cut along the axis, the radius of the open face was now different from core to core. Consequently the production curves should have significantly different shapes. It can be seen that this is actually the case and imbibition from a small radius hole outwards is almost linear. The reason is that most of the pressure drop occurs close to the inner open boundary and so the front position makes little difference to the production rate.

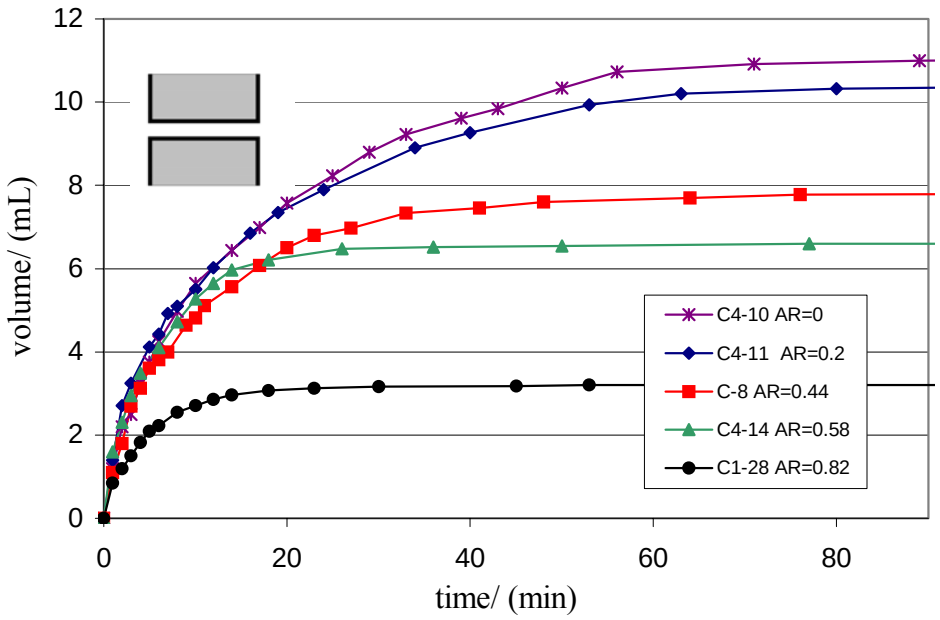

Figure 7-14. Production volume *vs* time for imbibition into cores with all faces except the outer surface sealed.

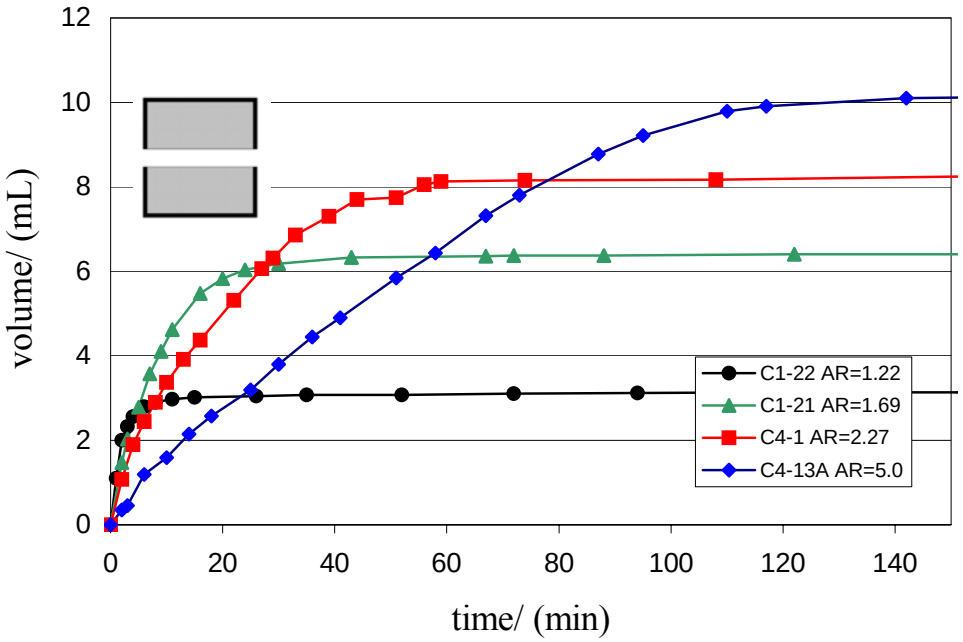

Figure 7-15. Production volume *vs* time results for imbibition into cores with all faces except the surface of the axial hole in the core sealed. Note that for the highest aspect ratio imbibition is almost linear with time.

Results for combined radial inwards and outwards imbibition are shown in Fig. 7-16. Note that, as would be expected, the time taken for imbibition to be completed is much shorter.

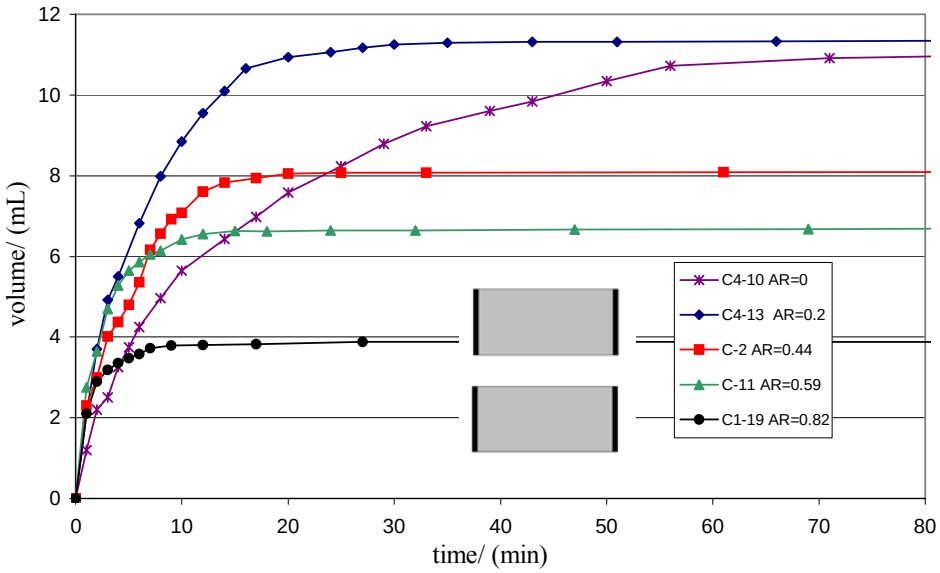

Figure 7-16. Production volume vs time results for cores with both ends closed. Imbibition takes place for all except C4-10 from both the inside hole and the outside surface. Consequently imbibition is much faster.

Interpretation of experimental results.

The experimental results need to be compared with the predictions of the theory. This is not as simple as it seems. The first question is whether or not the theory can match the **shape** of the production curve. The second question is whether the physical properties of the rock-oil-brine system predicted by the different scale factors are **consistent** between the linear, radial inwards and radial outwards experiments.

Fractional production can be determined for every experiment. This fraction can be inserted into the relevant functions relating time to fractional production (Eq. 7-36 and Eq. 7-37) and a time (multiplied by a constant factor) determined. Let the time calculated from f be t_f.

For linear imbibition Eq. (7-187) rearranges into

$$t_{f,\text{Linear, Mason}} = \sqrt{\frac{\varphi}{2K}} \frac{\left(S_{\text{wf}} - S_{\text{wi}}\right)}{MC_{\text{spread}}\sigma} L_{\text{max}}^2 f^2 \qquad (7\text{-}40)$$

and for the Ma-Ruth function

$$t_{f,\text{Linear,Ma}} = C_{\text{Ma}} \sqrt{\frac{\varphi}{K}} \frac{\sqrt{\mu_{\text{w}}}\mu_{\text{nw}}}{\sigma} L_{\text{max}}^2 f^2 \qquad (7\text{-}41)$$

where C_{Ma} is a constant. Let

$$G_{\text{Mason}} = \sqrt{\frac{\varphi}{2K}} \frac{\left(S_{\text{wf}} - S_{\text{wi}}\right)}{MC_{\text{spread}}\sigma} \qquad (7\text{-}42)$$

and

$$G_{\mathrm{Ma}} = C_{\mathrm{Ma}} \sqrt{\frac{\varphi}{K}} \frac{\sqrt{\mu_{\mathrm{w}}}\,\mu_{\mathrm{nw}}}{\sigma} \qquad (7\text{-}43)$$

As functions of f, Eq. 7-40 and Eq. 7-41 differ only by the arbitrary constants G_{Mason} and G_{Ma}. Both Equations 7-40 and 7-41 predict that the fraction imbibed during linear imbibition varies as the square root of time. This is not surprising because the driving pressures are constant but the resistances to flow vary as the distance that the front has advanced. In Equations 7-40 and 7-41 the core length is a parameter and this is best incorporated with f. Thus a plot of $L_{\max}^2 f^2$ versus the actual time for the fractional production f should be a straight line. Actually, because the production varies as the square root of time, it is better to take the square root of both axis variables because this spreads out the experimental points better. We thus have

$$L_{\max} f = \frac{\sqrt{t_{f,\mathrm{Linear,\,Mason}}}}{\sqrt{G_{\mathrm{Mason}}}} \qquad (7\text{-}44)$$

and

$$L_{\max} f = \frac{\sqrt{t_{f,\mathrm{Linear,\,Ma}}}}{\sqrt{G_{\mathrm{Ma}}}} \qquad (7\text{-}45)$$

The y-axis is proportional to the oil produced. Results showing $L_{\max} f$ plotted against the square root of the experimental time are shown in Fig. 7-17.

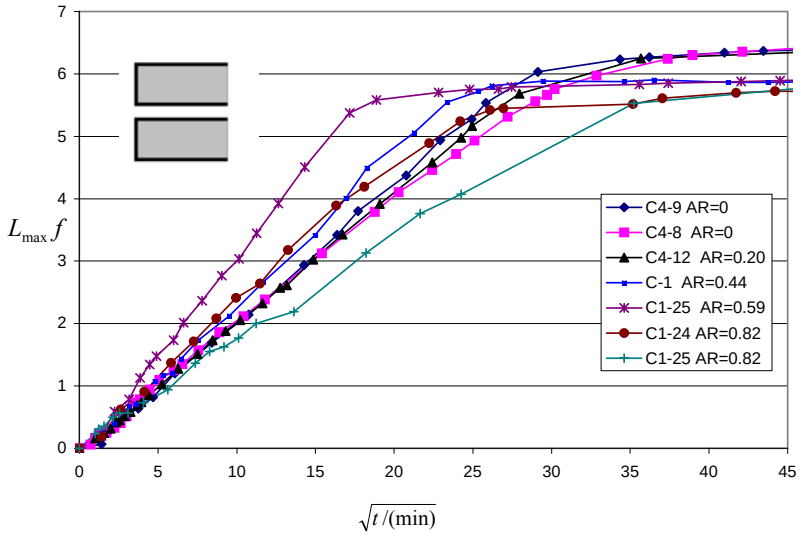

Figure 17. Results for linear imbibition plotted as $L_{\max} f$ *vs* the square root of the experimental time. The straight lines for the initial parts of the curves are predicted by theory. If all of the cores had identical properties, all the curves should fall on the same straight line. The greatest deviations are for cores which are near to a shell (aspect ratio 0.59 and 0.82) possibly because of the limited volume and associated inhomogeneities.

Figure 7-18 shows the results for linear imbibition with both ends open plotted in the same format but with the y-axis plotted as $L_{\max} f/2$ to allow for the effective length of the cores being halved. Again, the plots are all straight lines. However, although the majority of the gradients are

the same, the one for C4-11A is significantly different. There are two open faces for these cores and thus the possibility that imbibition will predominantly take place at one face and production from the other. The equations for flow indicate that ahead of the front there is a constant pressure in the non-wetting phase. This dead-end pressure drives the non-wetting phase back through the wetting phase and overcomes the capillary back pressure at the open face. When there are two open faces it may be that the capillary back pressures at the open faces are not equal or, because of inhomogeneity in the core, the permeability may not be evenly distributed. In both of these cases the rate of frontal advance will not be symmetric between the core ends. The production pattern should still vary linearly with the square root of time, but the gradient will be different.

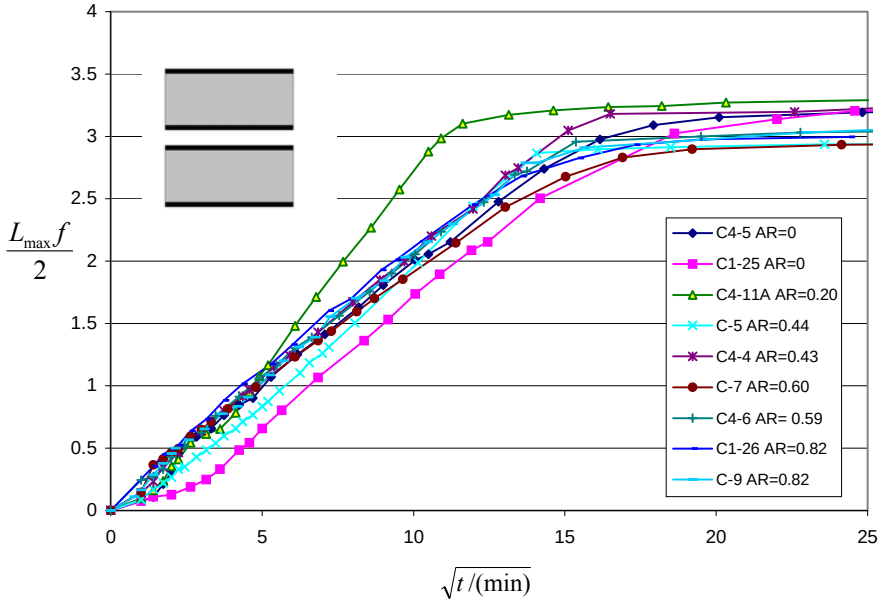

Figure 7-18. Results for linear imbibition with both ends open plotted as $L_{max} f/2$ *versus* the square root of the measured time. The scale factor allowing for the different effective length has been incorporated and so ideally the gradients of these functions should be the same as in Fig. 7-17. All of the scale factors predict that these functions should be straight lines.

The same method can be followed for radial imbibition. Now, however, the Ma, Ruth and Mason functions give different predictions. Eq. 7-36, gives R_f as a function of f

$$R_f^2 = R_{open}^2 - f\left(R_{open}^2 - R_{closed}^2\right) \tag{7-45}$$

Then

$$t_{f,Ma} = C_{Ma}\sqrt{\frac{\varphi}{K}}\frac{\sqrt{\mu_w}\mu_{nw}}{\sigma}\frac{\left(R_{open}-R_f\right)^2}{2}\left(1+\frac{R_f}{R_{open}}\right) \tag{7-46}$$

$$t_{f,Ruth} = C_{Ma}\sqrt{\frac{\varphi}{K}}\frac{\sqrt{\mu_w}\mu_{nw}}{\sigma}\frac{\left(R_{open}-R_f\right)^2}{3}\left(1+2\frac{R_f}{R_{open}}\right) \tag{7-47}$$

and

$$t_{f,Mason} = \sqrt{\frac{\varphi}{2K}}\frac{\left(S_{wf}-S_{wi}\right)}{C_{spread}M\sigma}\frac{1}{2}\left(R_{open}^2 + 2R_f^2\ln\frac{R_f}{R_{open}} - R_f^2\right) \tag{7-48}$$

If we define

$$F_{f,\text{Ma}}^2 = \frac{\left(R_{\text{open}} - R_f\right)^2}{2}\left(1 + \frac{R_f}{R_{\text{open}}}\right) \tag{7-49}$$

$$F_{f,\text{Ruth}}^2 = \frac{\left(R_{\text{open}} - R_f\right)^2}{3}\left(1 + 2\frac{R_f}{R_{\text{open}}}\right) \tag{7-50}$$

$$F_{f,\text{Mason}}^2 = \frac{1}{2}\left(R_{\text{open}}^2 + 2R_f^2 \ln\frac{R_{\text{f}}}{R_{\text{open}}} - R_f^2\right) \tag{7-51}$$

then the squares of these F factors are proportional to the appropriate times ($t_{f,\text{Ma}}, t_{f,\text{Ruth}}, t_{f,\text{Mason}}$). Thus plotting the squares of the F factors against the actual experimental times for the same fractional production, *f,* should give straight lines through the origin. Again, to spread out the data points approximately with the volume of oil produced, it is better to plot the square roots of both axis variables. The results should still be straight lines.

Figure 7-19 shows the results for radial inwards imbibition. In order to generate these plots, the experimental fractional productions, *f*, were used in Eq. 7-45 to determine a series of R_f's. Then these value of R_f were used to calculate the three values of F_f using Eq. 7-49 to Eq. 7-51. All of the plots are generally linear. At short and even medium times there is not much to choose between the three functions. However, at longer times the differences are significant, especially for the low aspect ratio cores. Because the Mason factor is linear for the longest times for the low aspect ratio core, it is marginally the best.

Figure 7-20 shows the results for radial outwards imbibition. Again for the high aspect ratio core the Mason factor produces the closest approximation to linearity, but otherwise there is not much difference between them, and virtually no difference at short times.

Results for the two ends closed cores which had simultaneous radial inwards and outwards imbibition were more difficult to analyse. Consequently they have only been interpreted using the Mason function. Essentially two versions of Eq. 7-37 were used, one for the outer front position and the other for the inner front position but with the times to reach these positions equal. Also, the fraction filled depends on the positions of both fronts. Consequently, for a fixed fraction filled, an iterative routine calculated the position of the two fronts and also the resulting time. Knowing the position of the front associated with an open face enabled $F_{f,\text{Mason}}$ to be calculated using Eq. 7-51. Figure 7-21 shows the results. They are, again, except for the high aspect ratio core, close to being straight lines with the same gradient.

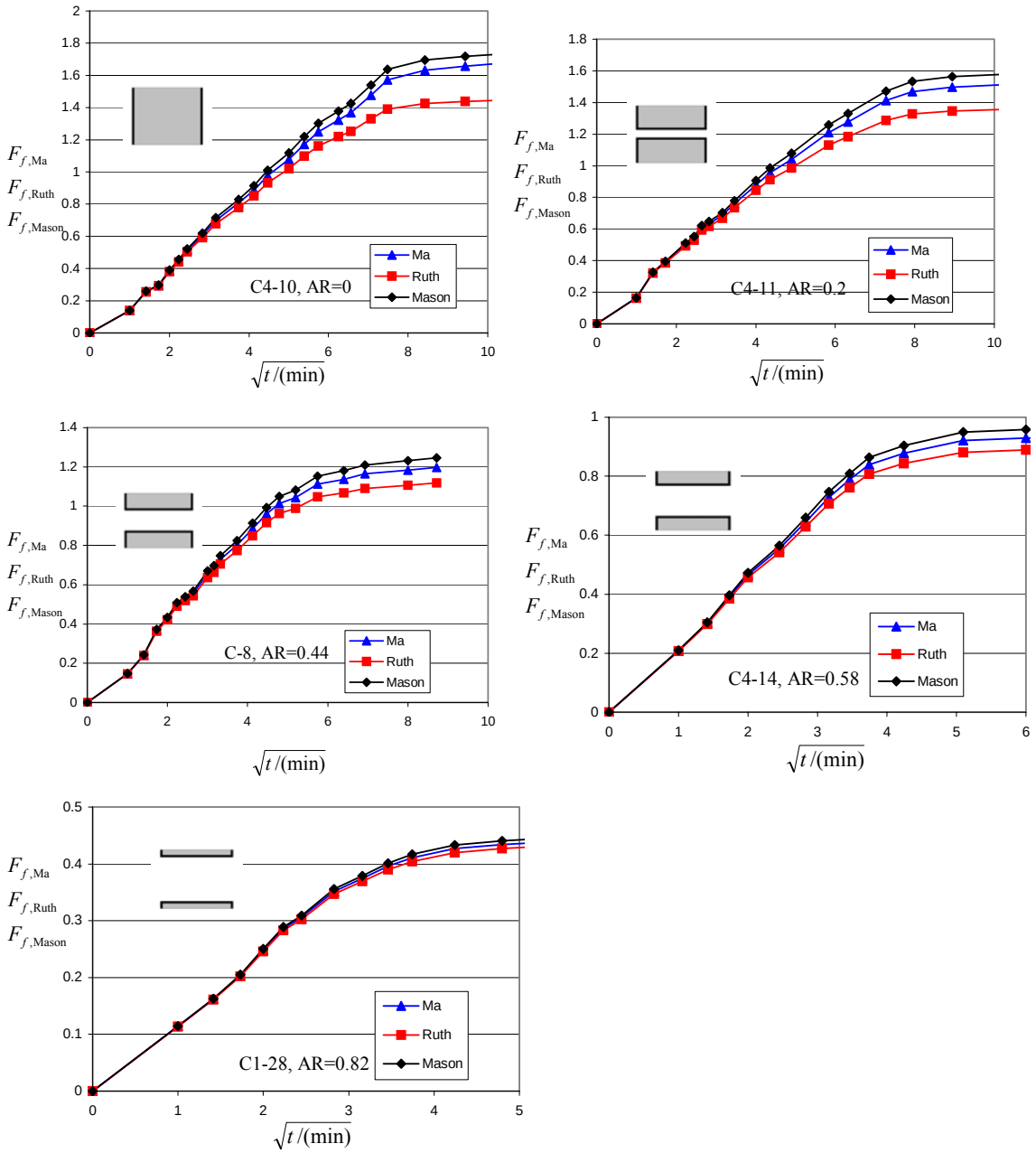

Figure 7-19. Comparison of the three functions for radial inwards imbibition for cores with five different aspect ratios. The gradients are all similar and close to the gradients for linear imbibition in Figs 7-17 and 7-18. The Mason function is closest to linearity. Only the gradient for imbibition with an aspect ratio of 0.82 differs significantly, it being too low by a factor of about 2. Because it is a thin shell (it was about 5mm thick) the leading part of the imbibition front may reach the closed boundary before the front is fully developed.

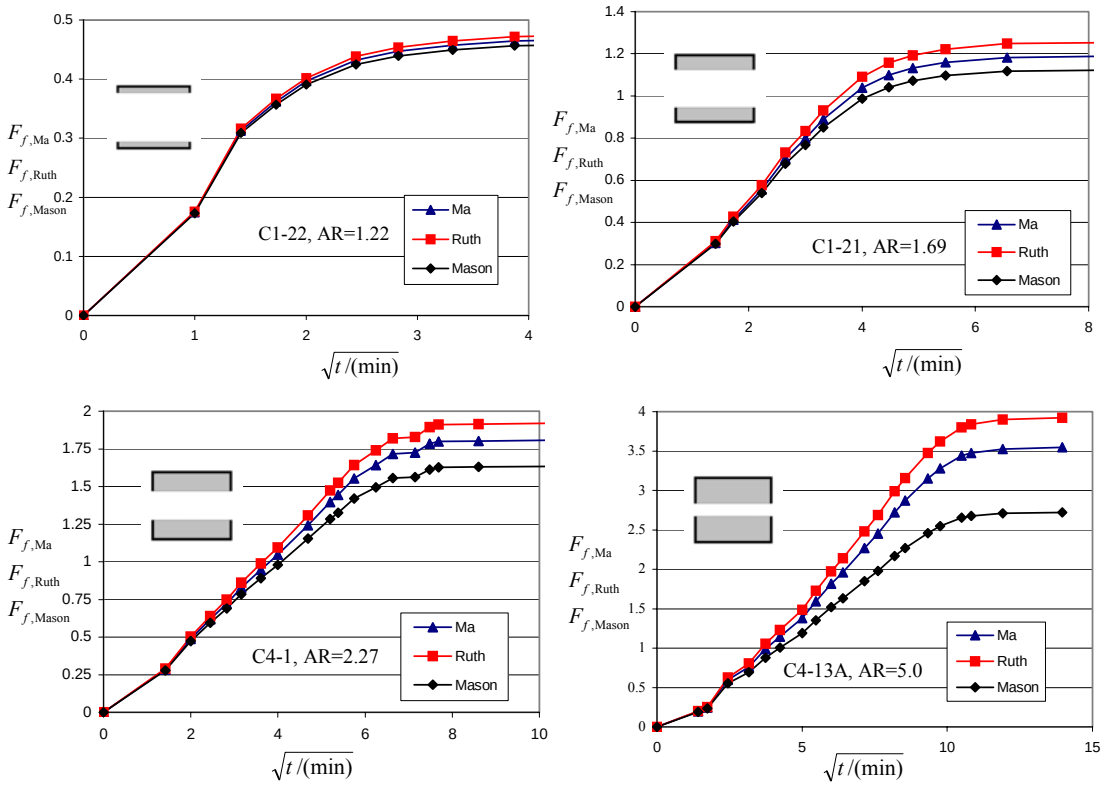

Figure 7-20. Radial outwards imbibition for cores with four different aspect ratios. There are only significant differences between the three functions for the high aspect ratio core (AR 5.0).

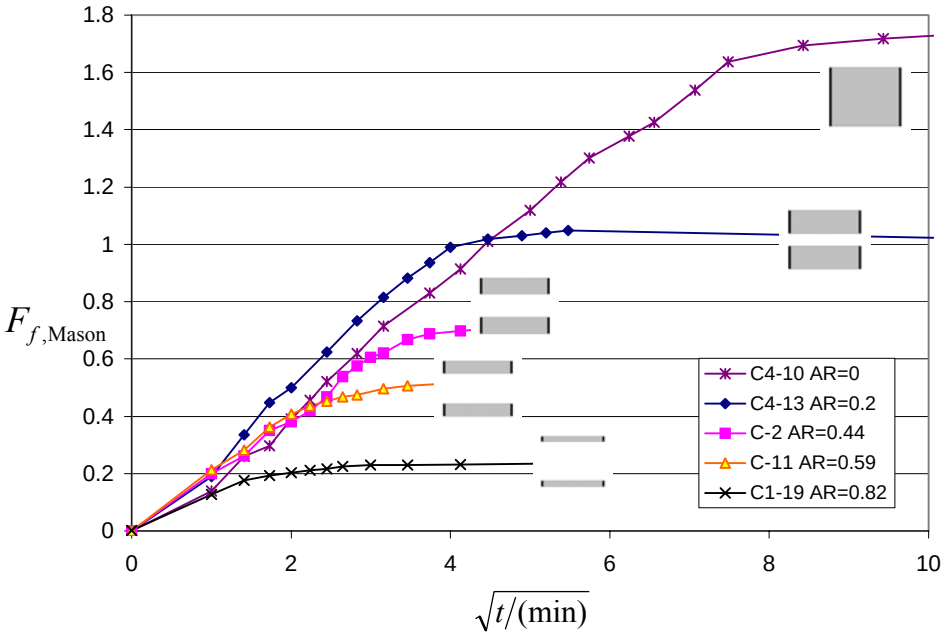

Figure 7-21. Results for both ends closed. The analysis is more difficult for this case because there are two fronts moving radially in opposite directions at different different places and at different rates. Except for the most extreme aspect ratio (0.82), the results give close-to straight lines of almost the same gradient. Some times are very short, making the experiments relatively inaccurate, especially for high aspect ratios. Core C4-10 has no hole in the middle (the results are also in Fig. 7-19). The square of the reciprocal of the gradients is about 20 for all of these cores, similar to Figs 7-17 to 7-20.

The reciprocal of the squares of the gradients of all of the functions for all of the results were calculated. These are typically gradients for about 75% of the recovery. For Figs 19 to 21 one might arguably subtract about half a minute (or a quarter, when squared) from the start times. These reciprocal gradients are the *G* values (Eqs. 7-42 and 7-43) and ideally all of these gradients would be the same. A general gradient has been taken for both the linear situations. However, the spread of the experimental values for linear imbibition does give an indication of the variability between the cores. The squares of the gradients are shown on Fig. 7-22 with the 'both ends closed' results omitted because they were only calculated for the Mason function and the aspect ratio varies with the predicted position of the no-flow boundary. The aspect ratio of 1 covers all of the linear imbibition results (one end or both ends open).

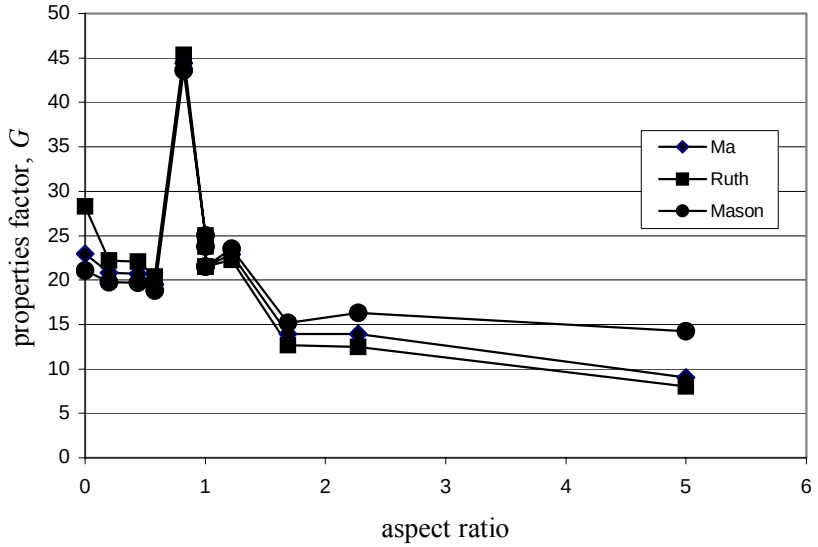

Figure 7-22. Comparison between the squares of the reciprocals of the gradients of Figs 7-17 to 7-20. These gradients are the *G* factors defined by Eqs. 7-42 and 7-43. Because they are properties of just the rock and fluids, they should, if the shape factor is correct, ideally all have the same value. Because it gives the most consistent *G* factor, the Mason scale factor probably the best of the three. The value for an aspect ratio of 0.82 which is too high by a factor of two. This is probably because it is only a thin shell about 5mm thick and has relatively little area open to imbibition which makes it subject to significant error.

In order to test how well the Mason function fits the shape of the production curves, the amount of oil produced as a function of time was calculated for all of the radial outwards experiments using a fixed value of 15 for the factor. The results are shown on Fig. 7-23. The early time data shows a reasonable fit except for AR=5. The function over-predicts production at short times. The linear and radial inwards production curves do not vary much in shape and are not shown.

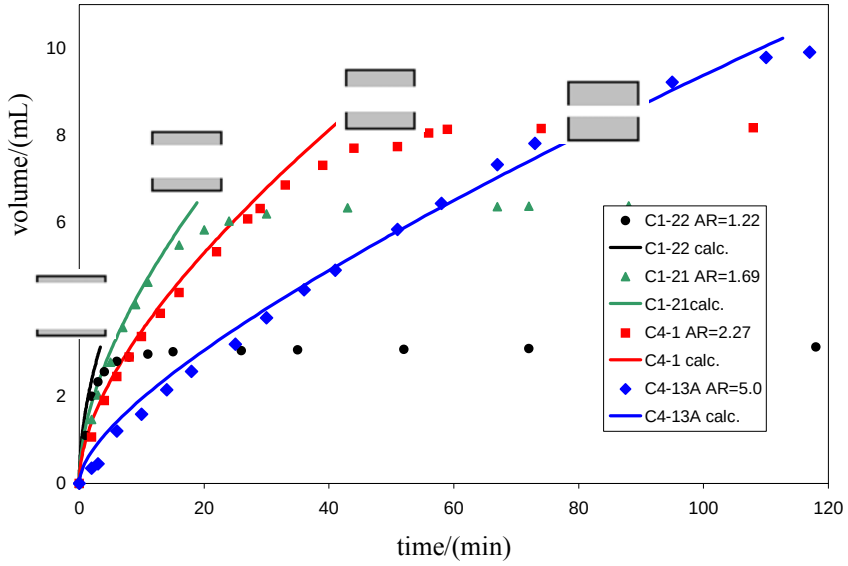

Figure 7-23. Comparison between experimental measurements and calculated values for radial outwards imbibition. Except for an aspect ratio of 5 the fits are quite good for the first 70% of the volume imbibed.

Discussion

The properties factor G can be obtained from the squares of the reciprocal gradients of the Mason fits in Figures 17-21. Ideally, because the same rock and fluid has been used throughout, all of these gradients should be the same. Set against this is the vast range of times for imbibition to be virtually complete; 2 minutes for the fastest and 1000 minutes for the slowest. Figure 24 shows the G values plotted against the core aspect ratio. Theory predicts that imbibition into one-end-open and two-ends-open cores should be independent of the aspect ratio. However, even for these geometries it can be seen that there is considerable scatter. The aspect ratio 0.82 gives the biggest spread. The values for radial outwards imbibition are marginally lower than the values for radial inwards imbibition. However, overall, the intrinsic variability between experiments seems to be greater than the errors incurred by differences in the shape factors. The cores have a range of volumes and this may go some way to explaining the variability. Also the capillary back pressure required to force oil from the cores is produced by the biggest connected pores at the open face and, statistically, this will probably depend on the surface area of the cores.

If we take an overall average value for G of about 20 then Eq. 7-42 gives

$$G_{\text{Mason}} = \sqrt{\frac{\varphi}{2K}} \frac{\left(S_{\text{wf}} - S_{\text{wi}}\right)}{MC_{\text{spread}}\sigma} \qquad (7\text{-}42)$$

The dimensions of G are TL^{-2}. Converting into internally consistent units and taking typical values for porosity and permeability gives

$$\frac{1}{M\mu_w} = \frac{1}{k_{rw}} + \frac{\mu_{nw}}{\mu_w k_{rnw}} \approx 1000 C_{spread} \qquad (7\text{-}52)$$

The viscosity ratio was about 3.5. Using the data of Li *et al* (2006) the value of C_{spread} can be estimated to be between 0.5 and 1. Consequently k_{rw} cannot be less than 0.002 and k_{rnw} cannot be less than 0.007. If k_{rw} and k_{rnw} are about equal then they will be about 0.009. Of course if C_{spread} is less or the capillary pressure at the front is not determined by the Leverett radius (and interfacial tension) then the relative permeabilities will be higher.

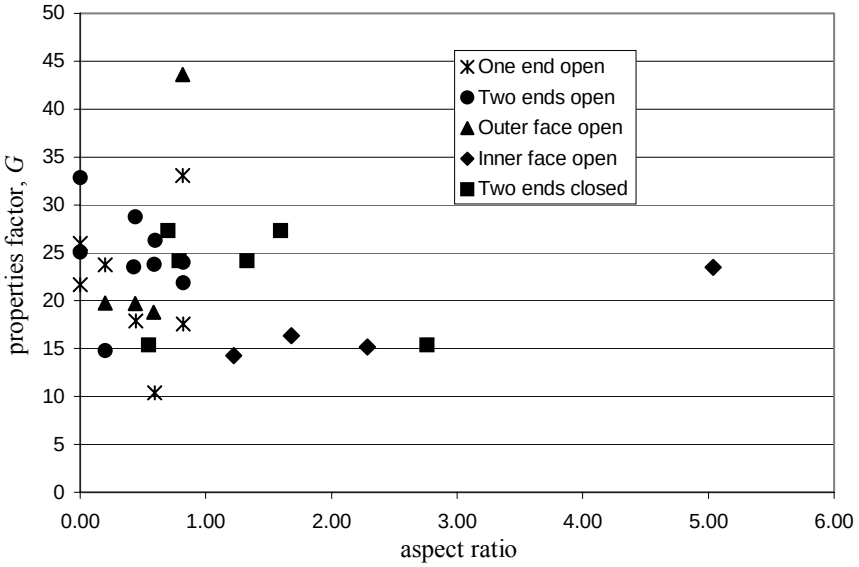

Figure 7-24. The properties factor *G* plotted against aspect ratio. Ideally, because the rock and fluids are the same, the value of *G* should be constant. It seems that the widest spread of values is for the cores with an aspect ratio of 0.8. These are only a thin shell and this may account for the spread of results.

The *G* factors are plotted against the surface area open for imbibition in Fig 7-25. It can be seen that the most consistent values are obtained for radial imbibition (especially inwards), provided that results for aspect ratio 0.82 are ignored. This implies that there is a critical thickness certainly greater than 0.5mm and maybe less than 15mm, above which consistent results are obtained and below which imbibition seems to occur more slowly. Also, there seems to be a critical area for the open face of about 50 square cm. Exceeding this seems to give more-consistent results. It may be that at least this area is required to give access to the largest pores and thus the lowest and most-consistent capillary back pressure. With too little area the capillary back pressure will likely to be too high with the result that imbibition will be slower, and thus *G* higher.

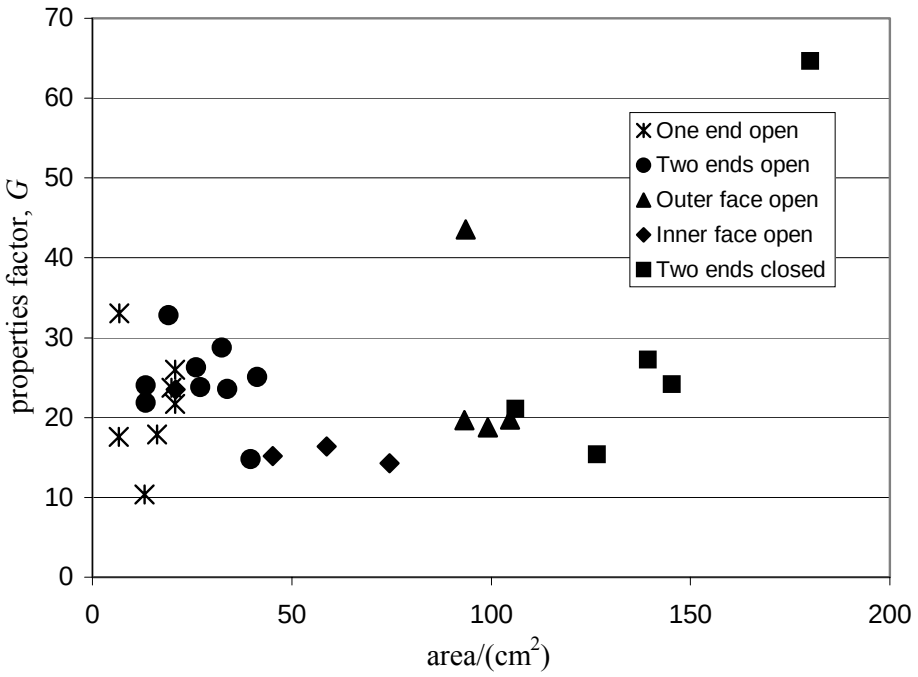

Figure 7-25. The properties factor *G* plotted against the area open to imbibition. The most consistent values occur with a surface area between 50 and 100 cm^2 and, from Fig. 25, core thickness greater than 15 mm. The two highest values for *G* come from cores with an aspect ratio of 0.82 which are only 5mm thick.

References

Behbahani, H.S., Donato, G.D. & Blunt, M.J., 2006, Simulation of counter-current imbibition in water-wet fractured reservoirs, J. Petroleum Science & Engineering, **50**, 21-39.

Cil, M. & Reis, J.C., 1996, A multi-dimensional, analytical model for counter-current water imbibition into gas-saturated matrix blocks, *J. Petroleum Science & Engineering*, **16**, 61-69.

Fischer, H. & Morrow, N.R., 2005, Spontaneous imbibition with matched viscosities, SPE Preprint 96812, SPE Annual Technical Conference, Dallas, Texas, 2005.

Fischer, H. & Morrow, N.R., 2006, Scaling of oil recovery by spontaneous imbibition for wide variation in aqueaous phase viscosity with glycerol as the viscosifying agent, *Journal of Petroleum Science and Engineeering*, **52**, 35-53.

Le Guen, S.S. & Kovscek, A.R., 2006, Nonequilibrium effects during spontaneous imbibition, *Transport in Porous Media*, **63**, 127-146.

Li, Y., Morrow, N.R. & Ruth, D., 2003, Similarity solution for linear counter-current spontaneous imbibition, *Journal of Petroleum Science and Engineering*, **39**, 309-326.

Li, Y, Ruth, D., Mason, G., & Morrow, N.R., 2006, Pressures acting in counter-current spontaneous imbibition, *Journal of Petroleum Science and Engineeering*, **52**, 87-99.

Mattax, C.C. & Kyte, J.R., 1962, Imbibition oil recovery from fractured, water drive reservoirs, *Society of Petroleum Engineers Journal*, June 1962, 117-.

Ma, S., Morrow, N.R. & Zhang, X., 1997, Generalized scaling of spontaneous imbibition data for strongly water-wet systems, *Journal of Petroleum Science and Engineeering*, **18**, 165-178.

Morrow, N.R. & Mason, G., 2001, Recovery of oil by spontaneous imbibition, *Current Opinion in Colloid & Interface Science*, **6**, 321-337.

Pirson, S., 1958, *Oil Reservoir Engineering*, McGraw-Hill New York.

Ruth, D., Mason, G. & Morrow, N.R., 2003, A numerical study of the influence of sample shape on spontaneous imbibition, Proceedings of the Society of Core Analysts Symposium, Pau, SCA2003-16, 1-12.
Washburn, E.W., 1921, The dynamics of capillary flow, Physical Review, **17**, 273-283.
Yildez, H.O., Gokmen, M, & Cesur, Y., 2006, Effect of shape factor, characteristic length, and boundary conditions on spontaneous imbibition, *J. Petroleum Science & Engineering*, **53**, 158-170.
Zimmerman, R.W., Bodvarsson, G.S. & Kwicklis, E.M., 1990, Absorption of water into porous blocks of various shapes and sizes, *Water Resources Research*, **26**, 2797-2806.

Task 8. *Application of network/numerical model to mixed wet rocks.*

Experiments that illustrate and quantify the basics of co- and countercurrent spontaneous imbibition have been conducted in a series of simple model pore systems. The fundamental pore geometry is a rod in an angled round-bottomed slot with the rod touching a capping glass plate. The capillaries thus formed by the surfaces of the slot, rod and plate do not have circular cross-sections but more complicated geometric structures with angular corners. The tubes formed at each side of the rod connect at both ends. A viscous, refined oil was applied from one end. For co-current experiments, the opposite end was left open to the atmosphere and oil imbibed into both tubes. For countercurrent experiments the opposite end was sealed and connected to a sensitive pressure transducer. Oil imbibed into the smaller capillary and expelled air as a series of bubbles from the end of the larger capillary. Bubble snap-off was observed to be rate-dependent and occurred at a lower curvature than that of the cylindrical meniscus that just fits inside the tube. Only the corners of the larger capillary filled with oil during countercurrent imbibition. Meniscus curvatures were calculated using the Mayer and Stowe-Princen method and were compared with actual values by measuring the capillary rise in the tubes; agreement was close. A simple model for co-current and countercurrent imbibition has also been developed and the predictions compared with the experimental results. The model results were in agreement with the experiments. The experiments demonstrate that the capillary back pressure generated by the interfaces and bubbles in countercurrent imbibition can slow the process significantly.

Introduction of Application of network/numerical model to mixed wet rocks.

A key process in the production of oil from fractured reservoirs is spontaneous imbibition. Such spontaneous imbibition may be either co-current or countercurrent, the second being more common. The main difference between the two mechanisms for imbibition is the direction of flow. In a co-current displacement the wetting and the non-wetting fluids move in the same direction with the non-wetting phase being pushed out ahead of the wetting phase. In countercurrent imbibition the phases move in opposite directions. The flows of both phases require a pressure gradient to drive them and, because the flows of each phase are in opposite directions, the pressure gradients have to be in opposite directions as well (Reis and Cil, 1993; Cil and Reis, 1996; Li et al., 2003). In general, the rate of co-current imbibition is about four times faster than that of countercurrent imbibition.

The physics of immiscible displacement in porous media has been simulated extensively by many researchers using a bundle of independent capillary tubes as the model (Nicholson,

1971; Nicholson, 1973; Lenormand et al., 1988; Dullien, 2000). In some of these models, the capillaries are uniform and identical, while in others they are uniform but have different diameters. The most important feature of these models is that there is no interaction between the tubes. Therefore the flow within each tube is independent of the others. The effect is that the menisci in the larger tubes advance faster than the ones in the smaller tubes. Dong and Dullien (1997) developed a capillary model for studying countercurrent flow, the model consisted of two capillary tubes connected by two short capillaries at the ends of the tubes. Only the two capillaries were involved. They analysed the saturation profiles during countercurrent imbibition inside the tubes. Dong et al ((1998) published a theoretical paper that introduced the concept of two parallel tubes for which the water in each tube at a single position along the tubes had the same pressure and the oil in each tube at the same position along the tubes had the same pressure. However, if one tube contained water and the other tube contained oil at the same position, the pressures of the two fluids could be different. They showed that, under these conditions, the invading fluid in the small tube always leads the invading fluid in the large tube. Ruth and Bartley (2003) extended this model by allowing for cross-flow without pressure-drop, what they termed "perfect cross-flow", between many tubes. They simulated co-current flow through sixty cross-connected capillaries of different sizes. In this situation, the menisci in the smaller tubes always lead the menisci in the larger tubes, the reverse of the independent tube model. The flow of a single phase in any tube is governed by the Hagen-Poiseuille equation. The Ruth and Bartley cross-flow model yielded results consistent with the Darcy model for two phase flow. Dong et al (2005; 2006) published further work that analyzed immiscible displacement through interacting capillaries; their results were consistent with those of Ruth and Bartley and with laboratory experiments using simple pore geometries.

As yet, the fundamentals of spontaneous countercurrent imbibition are still not completely understood. Our objective was to carry out experiments on some simple precise model systems and compare the results with theoretical predictions. Once the correct assumptions are known, they can be incorporated into continuum and pore network models so that they can better simulate imbibition. One key effect that we wished to observe was the actual process by which the non-wetting phase is ejected from the model pores; we also wished to measure the pressure that the process generates.

Design and capillary properties

Because the pores in oil reservoir rocks are normally angular, our model pores were designed to have angular corners. Based on past experience (Mason, 1983; Mason and Morrow, 1985; Mason et al., 2000), we decided to use a rod in a round-bottomed slot capped by a glass plate. The glass plate enabled the behavior of the menisci to be observed. The slot was not vertical but angled slightly so that the tubes formed on each side of the rod were of different shape and size. In co-current imbibition, both tubes filled together. In countercurrent imbibition, the small tube and the corners of the large tube filled and the displaced fluid (air) was driven out of the larger tube as a series of bubbles. Interconnection between the tubes can be made by making the slot deeper so that there is a gap between the rod and the plate. Experiments with this system will be reported separately.

The relationship between pore size and capillary pressure is straightforward for capillaries with circular cross-sections but is more complicated when the cross-section is irregular. For example, the meniscus in a tube with triangular cross-section is of complex shape because liquid is held in the corners of the tube (Mason et al., 2000). In order to model imbibition mathematically, the capillary properties of each of the two tubes have to be understood. The important properties are the meniscus curvatures at which the non-cylindrical pores fill or drain. The pore geometries of the experimental models used in this study are given by a rod in an angled slot with the rod touching (|AB|) or slightly spaced from a glass plate (Figure 8-1). Because the slot is angled, the tubes at the side of the rod have different sizes and shapes (Figure 8-1c). The situation gets more complicated if there is a gap, *d*, present between the rod and the plate, because, in effect, a third capillary structure can form in the gap and cross-flow between the two tubes can occur (Figure 8-1d). With a very large gap, the tube acts as a single capillary.

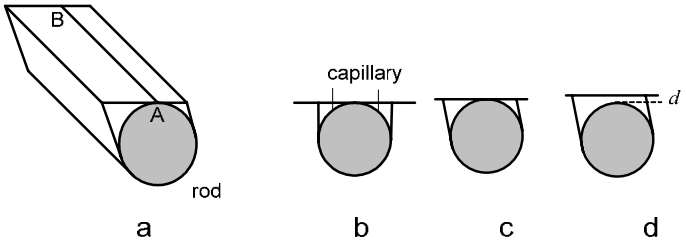

Figure 8-1. a) The pore geometry; a rod in an angled slot. b) Diagram of the cross-section of a rod in a square slot. c) Cross-section with the tube down one side larger than the other. d) Cross-section when the rod is spaced away from the capping glass plate. Three potential menisci are possible depending on the gap width: one large tube, one small tube and the meniscus in the gap.

The displacement curvatures of interfaces in uniform tubes of triangular, square or much more complex cross-section can be calculated using the Mayer and Stowe-Princen (MS-P) theory (Mayer and Stowe, 1965; Princen, 1969a; Princen, 1969b; Princen, 1970; Ma et al., 1996). The interface curvatures for menisci in complex cross-sections (three rods and a plate) such as those shown in Figure 1 have been calculated previously using the theory (Mason et al., 2000; Mason and Morrow, 1984). The behavior is quite complicated with, in some cases, as many as 3 coexisting menisci.

The curvatures of menisci in a rod-slot geometry with a general angle have been calculated using MS-P theory. The theory covers all cell angles but only cells with slot angles (β) of 65º, 75º and 85º were built for the experimental investigations. Typical relationships between meniscus curvatures and the width of the rod-plate gap are shown in Figure 8-2 for the various possible meniscus configurations.

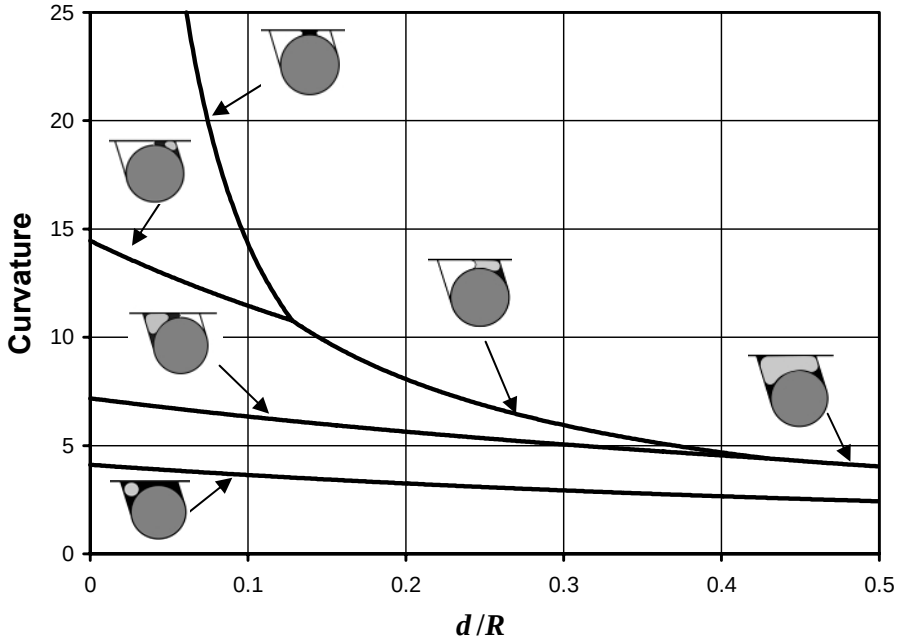

Figure 8-2. Meniscus curvatures normalised with respect to rod radius as a function of gap size, d, for a rod in an angled slot such as that shown in Figure 1(d). Slot angle β is 75º, d is the normalized gap size between the rod and the plate. R is the rod radius. The white areas show the tube space, black shows the wetting phase, and the grey shows the nonwetting phase, for each arc meniscus configuration.

As seen in Figure 8-2, for small gaps ($d/R < 0.13$) there are three menisci; a potentially very highly curved one in the gap between the rod and the plate, a less highly curved one in the small tube, and a meniscus in the large tube with about half of the curvature of the small tube meniscus. The lowest curvature indicated on Figure 8-2 is that of a cylindrical meniscus in the large tube; it corresponds to the curvature at which a bubble would snap off in this tube (Ma et al., 1996). For larger gaps ($0.13<d/R<0.42$), the distinct two-sided meniscus between the rod and the plate which separates the menisci in the large and small tube no longer exists. There is instead a capillary structure between the rod and the plate which is shared by the meniscus in the large tube and the meniscus in the small tube. For large spacings between the rod and the plate ($d/R>0.42$), this structure disappears and, apart from the arc menisci in the corners, the tube is spanned by a single meniscus.

Theoretical analysis

The experimental cell used to demonstrate the capillary properties of the rod-slot arrangement consists of two capillary tubes, one small (1) and one large (2), of the same length but of different cross-sections, plus the separate additional capillary. Initially all are completely filled with air (non-wetting phase) and at time $t=0$ the capillaries 1 and 2 are exposed to oil (wetting fluid) and oil partly fills the additional capillary. The interface in the additional capillary develops a pressure; this effect needs to be included in the analysis. General positions of the oil/air menisci during the process of oil displacing air are shown in Figure 8-3. During experiments the meniscus positions were video-taped so that the change in position of the interfaces with time could be determined.

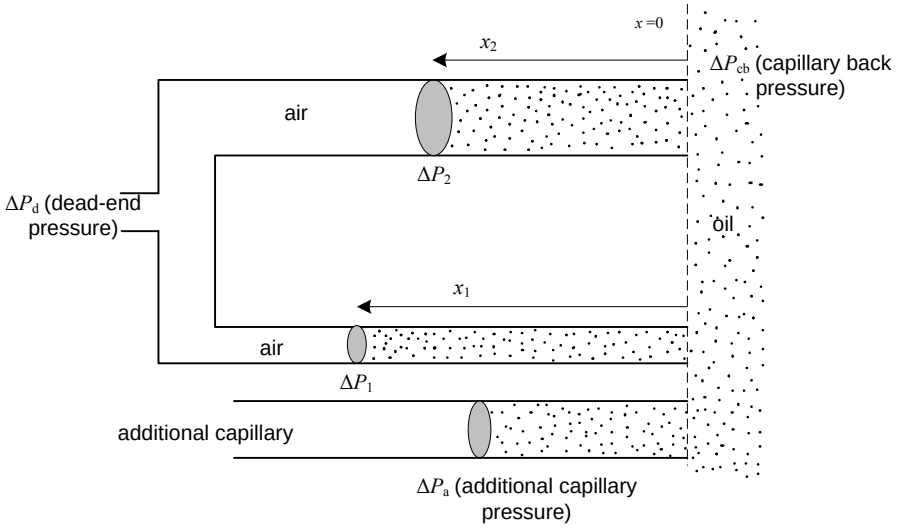

Figure 8-3. The positions of the oil/air menisci in the capillaries at time (*t*) in the process of oil displacing air.

The cell is operated horizontally to minimize the gravity effects. If both ends of the capillaries are open and the invading fluid is contacted with one end, then there will be co-current imbibition. The meniscus in the large tube will always be ahead of the meniscus in the small tube. Two menisci (one in each tube) will advance with the distance traveled varying as (time)$^{1/2}$ (Washburn, 1921). There are also arc menisci in the corners of the tubes. If the air-filled end is closed, then countercurrent imbibition occurs. The flows of each phase are now in opposite directions with oil flowing into the small tube and air out of the large tube. The curvature of the meniscus spanning each tube will equal to the local curvature of the arc menisci in the tube corners (the basis of the MS-P theory). Eventually, air will reach the oil end of the large tube and an air bubble will form from the center. The arc menisci in the corners are initially highly curved and their curvature decreases as they expand away from the corners. In the air-filled large tube, the curvature of the arc menisci near the oil end almost equals the curvature of the bubble leaving the tube center. When these arc menisci overlap the bubble will snap off. When the small tube is filled to the end with oil, imbibition will cease with the center of the large tube still filled with air. The rate at which imbibition occurs will depend on the sizes of the two tubes.

Theory of co-current imbibition

The theory for co-current imbibition is less complicated than for countercurrent imbibition. The relation between the distance that the meniscus advances, x, in terms of volumetric flow rate Q and time t is,

$$\bar{u} = \frac{dx}{dt} = \frac{Q}{A} \qquad (8\text{-}1)$$

where $\bar{u}$ is the average velocity and A is the cross-sectional area of the capillary. The cross-sectional area and the perimeters of the side capillaries for two tubes with a cell angle β are shown in Figure 8-4.

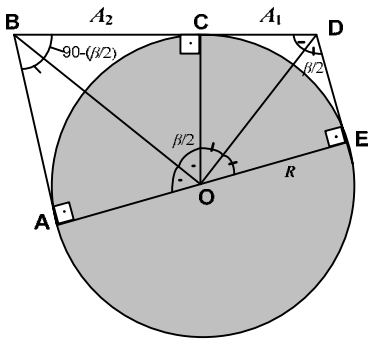

Figure 8-4. Cross-sections of capillaries.

$$A_1 = R^2 \tan(90-\beta/2) - [\pi R^2 (180-\beta)/360] \quad (8\text{-}2)$$

$$A_2 = [R^2 \tan(\beta/2)] - [\pi R^2 \beta/360] \quad (8\text{-}3)$$

$$S_1 = 2R\tan(90-\beta/2) + 2\pi R((180-\beta)/360) \quad (8\text{-}4)$$

$$S_2 = 2R\tan(\beta/2) + 2\pi R(\beta/360) \quad (8\text{-}5)$$

where A_1 is the cross-sectional area of the small capillary, A_2 is the cross-sectional area of the large capillary, S_1 is the perimeter of the small capillary, S_2 is the perimeter of the large capillary and R is the rod radius. For laminar flow, $\overline{u}$, is given by,

$$\overline{u} = \frac{dx}{dt} = \frac{k}{\mu}\delta^2 \frac{P}{x} \quad (8\text{-}6)$$

where δ is a dimension associated with the tube, μ is the fluid viscosity, x is the length, P is the pressure difference driving the flow and k is a shape factor. For co-current flow, the cell is open to the atmosphere so P is the difference between the pressure across the interface (ΔP) and the pressure developed by the additional capillary (ΔP_a) (see Equation 8-7).

$$\overline{u} = \frac{dx}{dt} = \frac{k}{\mu}\delta^2 \frac{(\Delta P - \Delta P_a)}{x} \quad (8\text{-}7)$$

Note that air is being displaced and, because the viscosity of air is so small, this takes virtually no pressure drop. The fluid imbibing into the tubes is drawn from the additional capillary, which, because of its large cross-section, also takes virtually no pressure drop. For a particular tube let $k\delta^2 = K$, a constant. Thus the variables can be separated giving,

$$\int_{x_0}^{x_t} x dx = \frac{K(\Delta P - \Delta P_a)}{\mu} \int_{t_0}^{t} dt \quad (8\text{-}8)$$

and

$$K_1 = \frac{(x_{1,t}^2 - x_{1,0}^2)\mu}{2(\Delta P_1 - \Delta P_a)(t-t_0)} \quad \text{and} \quad K_2 = \frac{(x_{2,t}^2 - x_{2,0}^2)\mu}{2(\Delta P_2 - \Delta P_a)(t-t_0)} \quad (8\text{-}9)$$

In Equation 8-9, the variables μ, $(\Delta P_1 - \Delta P_a)$, $(\Delta P_2 - \Delta P_a)$, K_1 and K_2 are all constants, so a plot of $(x_{1,t}^2 - x_{1,0}^2)$ and $(x_{2,t}^2 - x_{2,0}^2)$ vs $(t\text{-}t_0)$ should be a straight line, with a gradient of

$m_1 = \frac{2(\Delta P_1 - \Delta P_a)K_1}{\mu}$ for the small capillary and $m_2 = \frac{2(\Delta P_2 - \Delta P_a)K_2}{\mu}$ for the large capillary. In addition, eliminating $(t - t_0)$ from Equation 8-9 gives

$$x_{1,t}^2 - x_{1,0}^2 = \frac{(\Delta P_1 - \Delta P_a)}{(\Delta P_2 - \Delta P_a)} \frac{K_1}{K_2} (x_{2,t}^2 - x_{2,0}^2) \qquad (8\text{-}10)$$

In Equation 8-10, a plot of $x_{1,t}^2$ vs $x_{2,t}^2$ should be a straight line, with a gradient of $m = \frac{(\Delta P_1 - \Delta P_a)}{(\Delta P_2 - \Delta P_a)} \frac{K_1}{K_2}$ and intercept of $(x_{1,0}^2 - m x_{2,0}^2)$ since the variables $x_{1,0}^2$, $x_{2,0}^2$, K_1, K_2, $(\Delta P_1 - \Delta P_a)$ and $(\Delta P_2 - \Delta P_a)$ are constants.

In an experiment, the x values can be determined from time-spaced video images. The capillary pressure ($\Delta P_1, \Delta P_2, \Delta P_a$) can be measured in separate experiments and so the values of K_1 and K_2 can be determined. Because these factors depend only on the geometry of the capillaries, they will be the same for both co- and countercurrent imbibition. Therefore the co-current experiments can be used to obtain values for parameters in the countercurrent experiments which cannot otherwise be measured.

Theory of countercurrent imbibition

For countercurrent imbibition, the flow equation is the same as Equation 8-6 but the driving pressures are different. There is an additional pressure at the end of the cell which drives the countercurrent flow in the large tube but also slows the flow in the small tube. If ΔP_d is the pressure difference between atmospheric and that in the dead end then the pressure during flow in the small (tube 1) is

$$[\Delta P_1 - \Delta P_a - \Delta P_d] \qquad (8\text{-}11)$$

In the larger capillary, the pressure during the countercurrent flow is

$$[\Delta P_d + \Delta P_a - \Delta P_{cb}] \qquad (8\text{-}12)$$

where ΔP_{cb} is the capillary back pressure in tube 2. If the tube contains a meniscus then ΔP_{cb} will be ΔP_2. However, when the meniscus is not in the tube, it blows a bubble at the tube exit and the pressure ΔP_{cb} is less than ΔP_2 but it is still not zero. Eventually, the bubble snaps off and the meniscus retreats up the large tube. ΔP_{cb} then becomes equal to ΔP_2 again. The flow rates in the two tubes during countercurrent imbibition are

$$Q_1 = \bar{u}_1 A_1 = \frac{K_1}{\mu} A_1 \frac{[\Delta P_1 - \Delta P_a - \Delta P_d]}{x_1} \qquad (8\text{-}13)$$

and

$$Q_2 = \bar{u}_2 A_2 = \frac{K_2}{\mu} A_2 \frac{[\Delta P_d + \Delta P_a - \Delta P_{cb}]}{x_2} \qquad (8\text{-}14)$$

where x_1 and x_2 are the positions of the interfaces, $K_1 = k_1 \delta_1^2$ and $K_2 = k_2 \delta_2^2$. When $x_2 > 0$ then $\Delta P_{cb} = \Delta P_2$.

As the interface in the small capillary imbibes, the interface in the larger capillary tube moves in the reverse direction. The volumetric flow rates are equal.

$$Q_1 = Q_2 \tag{8-15}$$

giving (from Equations 8-13 – 8-15)

$$\frac{K_1}{K_2}\frac{A_1}{A_2}\frac{x_2}{x_1}[\Delta P_1 - \Delta P_a - \Delta P_d] = [\Delta P_d + \Delta P_a - \Delta P_{cb}] \tag{8-16}$$

and if $B = \dfrac{K_1}{K_2}\dfrac{A_1}{A_2}$ (8-17)

$$B\frac{x_2}{x_1}(\Delta P_1 - \Delta P_a - \Delta P_d) = \Delta P_d + \Delta P_a - P_{cb} \tag{8-18}$$

and, rearranging

$$\Delta P_d = \frac{B\dfrac{x_2}{x_1}\Delta P_1 + \Delta P_{cb}}{1 + B\dfrac{x_2}{x_1}} - \Delta P_a \tag{8-19}$$

If ΔP_{cb} equals ΔP_2, then ΔP_d can be eliminated from Equation 8-14 giving

$$\frac{dx_2}{dt} = \frac{K_2 A_2}{\mu x_2}\left[\left[\frac{B\dfrac{x_2}{x_1}\Delta P_1 + \Delta P_2}{1 + B\dfrac{x_2}{x_1}} - \Delta P_a\right] + \Delta P_a - \Delta P_2\right] \tag{8-20}$$

which rearranges into

$$x_1 dx_2 + Bx_2 dx_2 = \left[\frac{K_1 A_1}{\mu}(\Delta P_1 - \Delta P_2)\right]dt \tag{8-21}$$

where $\left[\dfrac{K_1 A_1}{\mu}(\Delta P_1 - \Delta P_2)\right]$ is constant (= D). Volumetric flows are equal in both capillaries, so

$$A_1 dx_1 = -A_2 dx_2 \tag{8-22}$$

Integrating Equation 8-21 gives

$$\frac{1}{2}B x_2^2 - \frac{1}{2}\frac{A_1}{A_2}x_1^2 = D\,t \tag{8-23}$$

Equation 8-23 shows that the relationship between (x_1^2, x_2^2) and t should be linear.

Experimental

Experiments were conducted for three model pore systems using a perfectly wetting oil. With the model pore system vertical, the capillary rise in each tube was measured and the

curvature of the menisci in each of the three tubes obtained. Next, with the pore system horizontal both co-current and countercurrent imbibition experiments were carried out.

Model Systems

The model is an aluminum block cell with a size 4cm x 11cm x 2cm. It has a round-bottomed angled slot precisely machined into the top surface by means of a ball ended milling cutter to exactly accommodate a steel rod (a drill blank) (Figure 8-5). To minimize gravity effects the cell is operated horizontally with a rod of 3.12 mm diameter. There is no hydraulic pathway beneath the rod. The slot is angled ($\beta = 65^{\circ}, 75^{\circ}, 85^{\circ}$) and the two capillaries of different sizes are completed by a glass plate above the rod.

The cell has two interconnected reservoirs, the outer (Reservoir I) and the inner (Reservoir II). Reservoir I is cylindrical, with a diameter and a depth of 1 cm. Reservoir II has an elliptical cross-section and is the same depth as Reservoir I. Reservoir II is connected to the end of the rod/slot arrangement. The glass plate covers the full length of the capillaries as well as all of Reservoir II and is secured with retainers and screws.

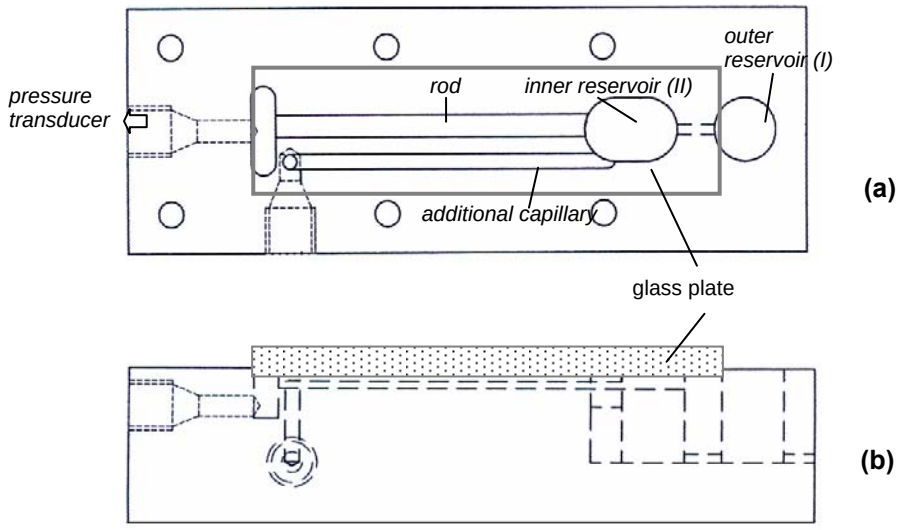

Figure 8-5. Sketch of the cell, (a) view fron the top (b) the view from the side.

There is an additional capillary running parallel to the rod from reservoir II and which eventually leads out to the atmosphere through the side of the cell. Its purpose is to maintain a constant pressure in Reservoir II. In our initial design, Reservoir II was open to the atmosphere and oil slowly leaked along the edge between the glass plate and the cell. This leakage lowered the level in Reservoir II and produced a drift in the measured pressures. The problem was solved by capping Reservoir II and adding the additional capillary. The interface in the additional capillary also gives a volume leeway in that the meniscus can move forward and backwards at constant capillary pressure.

At the opposite end of the capillaries to Reservoir II there is a small chamber with a pressure tap for connection to one side of a sensitive differential pressure transducer (Furness Model FCO 44). The signal from the transducer is monitored by a data logger. A T-connection is placed where the additional capillary opens to the atmosphere. One end of this T-connection connects to one side of the differential pressure transducer and the other is connected to atmosphere via a long length of tubing. This design reduced the effects of short-term pressure changes in the room (i.e. doors opening).

There is a slight depression ground into the glass plate just above the ends of the capillaries in Reservoir II which allows the bubbles formed during countercurrent imbibition to drift away after they have snapped off. Without this depression a successive bubble can fuse with its predecessor and trigger premature snap-off.

Fluids

For the imbibition experiments, both co-current and countercurrent, medicinal liquid paraffin was used to displace air. For the capillary rise experiments *iso*-octane was used . The densities of the liquids were measured using a pycnometer and the surface tensions using a surface tension balance (Model DB 2kS, White Electronics, WR, UK). The viscosity of paraffin was determined using a viscotester (ThermoHaake VT550, Haake, Germany). The properties of both liquids are given in Table 8-1.

Table 8-1. Properties of liquid paraffin and iso-octane.

solution	Density	Viscosity	surface tension
Liquid paraffin	0.83 g/cm^3	180 mPa.s	33.83 dyne/cm
Iso-octane	0.71 g/cm^3	-----	19.42 dyne/cm

Meniscus curvatures

When the rod touches the plate the system is basically a rod-in-an-angled-corner configuration for which the MS-P curvatures are known (Walsh, 1989). The capillary pressures for all of the menisci in the cells were measured by the capillary rise of *iso*-octane following the experimental procedure described by Mason and Morrow (1985). The actual capillary pressures for *iso*-octane and liquid paraffin are given in Table 8-2.

Table 8-2. Capillary pressures (in Pa) determined by capillary rise experiments for *iso*-octane (Iso.) and liquid paraffin (L.P.) in the rod-plate-contact cells.

Cell	ΔP_1		ΔP_2		ΔP_a	
	Iso.	L.P.	Iso.	L.P.	Iso.	L.P.
Slot angle β 85º	133.60	232.53	105.62	183.78	31.52	54.85
Slot angle β 75º	165.18	287.41	80.22	139.61	27.62	48.32
Slot angle β 65º	212.26	368.92	64.71	112.59	27.48	47.80

Normalized curvatures are compared with the MS-P theory in Figure 8-6.

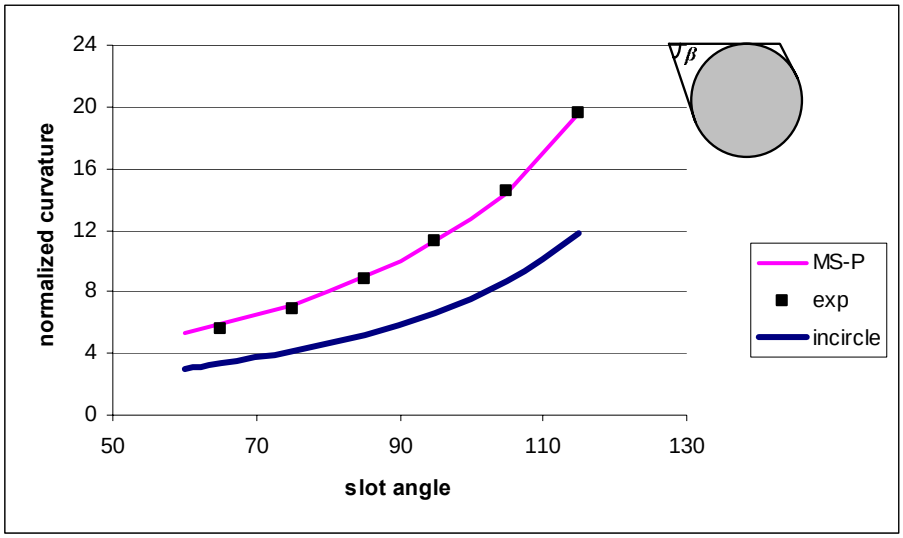

Figure 8-6. Comparison of measured curvatures with values calculated by MS-P method for the rod-in-angled corner geometry. Also shown is the incircle curvature (note that the insphere curvature would be double the incircle curvature).

Operation

Before the experiment began, the correct volume of liquid paraffin (determined by trial) was placed in Reservoir I. The liquid was then pushed from Reservoir I by means of a close-fitting piston into Reservoir II. As the liquid is pushed out of Reservoir I, the oil level rises in Reservoir II and finally reaches the capillaries. Excess oil flows into the additional capillary forming a meniscus until it stops. In addition, a meniscus forms in each capillary on each side of the rod and these start to advance. For co-current imbibition, the pressure transducer is not connected to the cell. Hence, one end of the capillaries is open to the atmosphere. During countercurrent imbibition the transducer is connected and it measures the pressure build-up of the air in the dead end (ΔP_d).

For the interfaces in the two tubes there are arc menisci that advance along the corners forming liquid wedges. Although their curvature is high, their hydraulic resistance is also high (Dong and Chatzis, 1995). Consequently, as the main terminal menisci (Mason and Morrow, 1987) move along the capillaries the arc menisci do not advance far, nor carry much liquid, ahead of the main menisci.

Results

Co-current imbibition

Single frames from an experiment involving co-current flow are shown in Figure 8-7. The menisci have been drawn over for clarity.

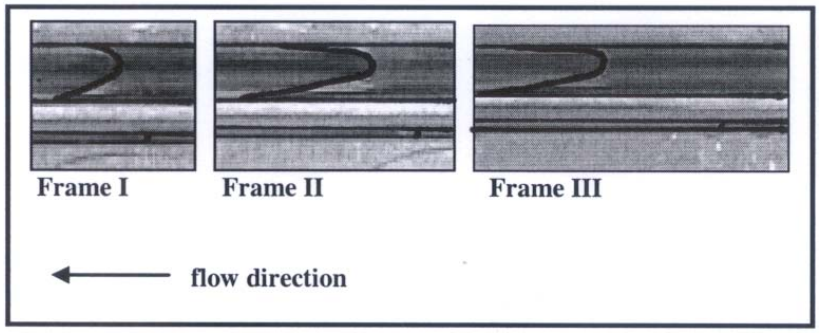

Figure 8-7. Single frames from an experiment involving co-current imbibition. Slot angle β is 75º. Note that small meniscus is always ahead of the larger meniscus.

Equation 8-9 predicts that a plot of $(x_{1,t}^2 - x_{1,0}^2)$ vs $(t - t_0)$ should be a straight line with the gradient depending on the hydraulic resistance shape factor *K*. The same is true for the other capillary tube. Figure 8-8 shows the result for all three cells.

The additional significance of the lines in Figure 8-8 being straight means that the capillary pressures generated by the menisci are constant, even though in each tube the velocity of advance varies considerably with time. The explanation is probably that the arc menisci in the corners always lead the main terminal meniscus. The significance is that in network models the interfaces are assumed to be quasi-static and generate a constant pressure. Figure 8-8 shows that this is probably a good approximation to the moving situation.

In addition, Equation 8-10 predicts that a plot of x_1^2 vs x_2^2 is a straight line. This plot is shown in Figure 8-9. It is interesting that the results for the 65º and 75º cells are almost coincident. This is because changes in the hydraulic resistance are almost compensated by changes in the capillary pressure.

Because the capillaries have noncircular cross-sections with corners, their true hydraulic resistances are difficult to estimate (Dong and Chatzis, 1995; Ransohoff and Radke, 1998). This is why the shape factor, *k*, in Equation 8-7 is needed. For flow through circular tubes the average velocity, $\bar{u}$, is given by Corey (1994)

$$\bar{u} = \frac{dx}{dt} = \frac{r^2}{8\mu}\frac{P}{x} \qquad (8\text{-}24)$$

The shape factor *k* is 1/8 for this case. The hydraulic radius of irregular capillaries (r_{hyd}) can be estimated from the ratio of the area to the perimeter (Corey, 1994; Sisavath et al., 2001; Patzek and Silin, 2001; Patzek and Kreistensen, 2001).

$$r_{hyd} = \frac{A}{S} \qquad (8\text{-}25)$$

where *A* is the cross-sectional area perpendicular to flow, and *S* is the wetted perimeter. The A_1, A_2, S_1 and S_2 values are given in Equations 8-2 – 8-5.

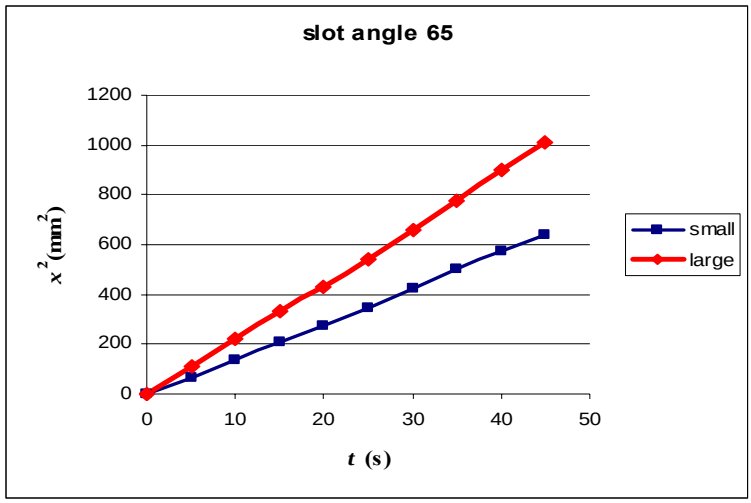

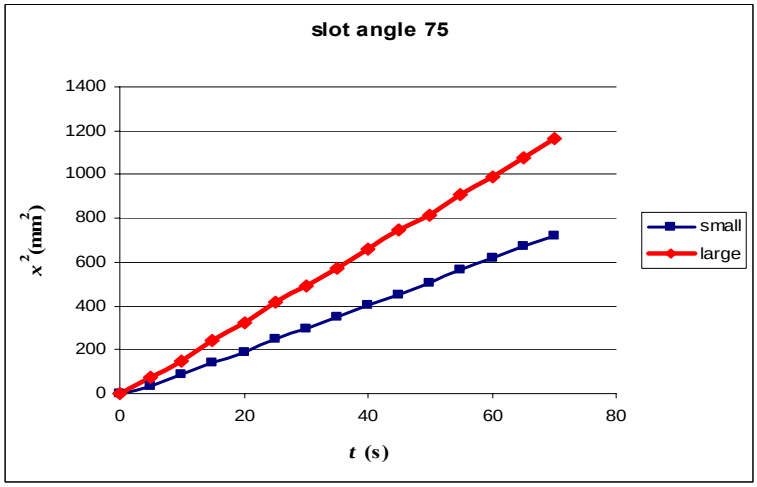

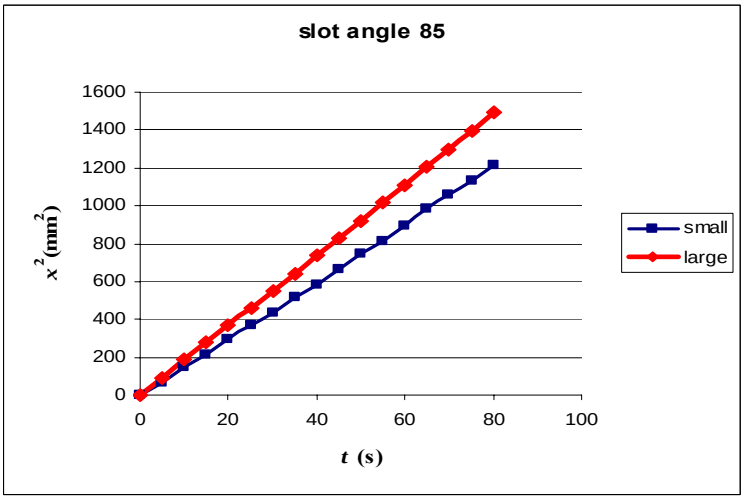

Figure 8-8. Plot of $(x_t^2 - x_0^2)$ vs $(t - t_0)$ for both capillaries in each cell. Theory predicts that the slope (*m*) should be equal to $m = \frac{2(\Delta P - \Delta P_a)K}{\mu}$ values and the lines should be straight.

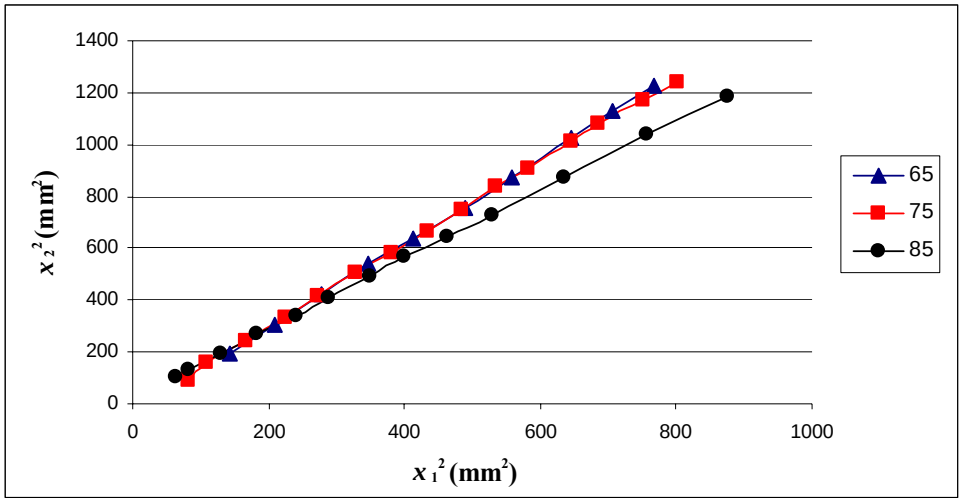

Figure 8-9. Plot of $x_{1,t}^2$ vs. $x_{2,t}^2$ for the cell with slot angles of 65º, 75º and 85º. Theory predicts that the relationship should be straight lines.

Using distance-time measurements for each cell (and Equation 8-24) the hydraulic radius value for each capillary was found. The measured and theoretical values (from Equation 8-25) are compared in Figure 8-10. Good agreement was found between the experimental and the theoretical hydraulic radii values.

Figure 8-10. Theoretical and experimental hydraulic radii value ratios at different slot angles (º). 'r_{hyd1}' is the hydraulic radius of the small capillary, 'r_{hyd2}' is the hydraulic of the large capillary.

Countercurrent flow

In counter- current imbibition, initially both interfaces advance, with the larger one leading. As the air is compressed, the large interface is pushed back by increasing air pressure until bubbles are blown from the large capillary tube. After each bubble snaps off, an interface advances a short way into the large capillary. Single frames from an experiment involving

bubble snap-off during a countercurrent flow are shown in Figure 8-11. The menisci have been drawn over for clarity.

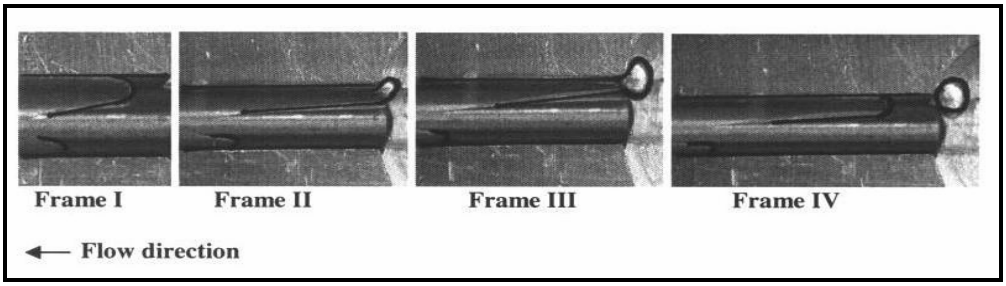

Figure 8-11. Countercurrent imbibition. A bubble is emerging from the large tube. After snap-off the meniscus invades the tube for some distance. Slot angle β is 75º.

At the beginning, before the oil is introduced into the capillaries, the differential pressure transducer shows a constant value of around 0 P_a. As the oil imbibes into the capillaries the pressure rises to the first positive peak. When the length of the large tube filled with oil decreases, the pressure drops slightly and then drops more rapidly as the bubble forms. Eventually the bubble snaps off and the air pressure rises back to almost the initial value and stays essentially constant until the next bubble starts to form. After the snap-off, the meniscus in the large tube appears to invade the tube for some distance but close observation shows that most of the liquid comes from drainage of the arc menisci until their curvature corresponds to that of the main meniscus. As the imbibition rate slows down, the time taken for bubble formation increases. This drop in rate is probably the cause of the slight increase in snap-off pressure of the later bubbles. With slower bubble growth the snap-off pressure moves closer to the curvature of a theoretical cylindrical meniscus within the tube.

When the meniscus forms in the additional capillary, it creates an additional capillary pressure between the atmosphere and the fluid which, in effect, shifts the zero indicated pressure of the transducer. This pressure is equal to ΔP_a and if this value is subtracted from the zero initial pressure, we obtain the 'absolute base pressure'. The pressure produced by the additional capillary was obtained from the capillary rise experiments (see Table 8-2). The data plot for the transducer readings (ΔP_d) of the cell with a slot angle of 85º is given in Figure 8-12.

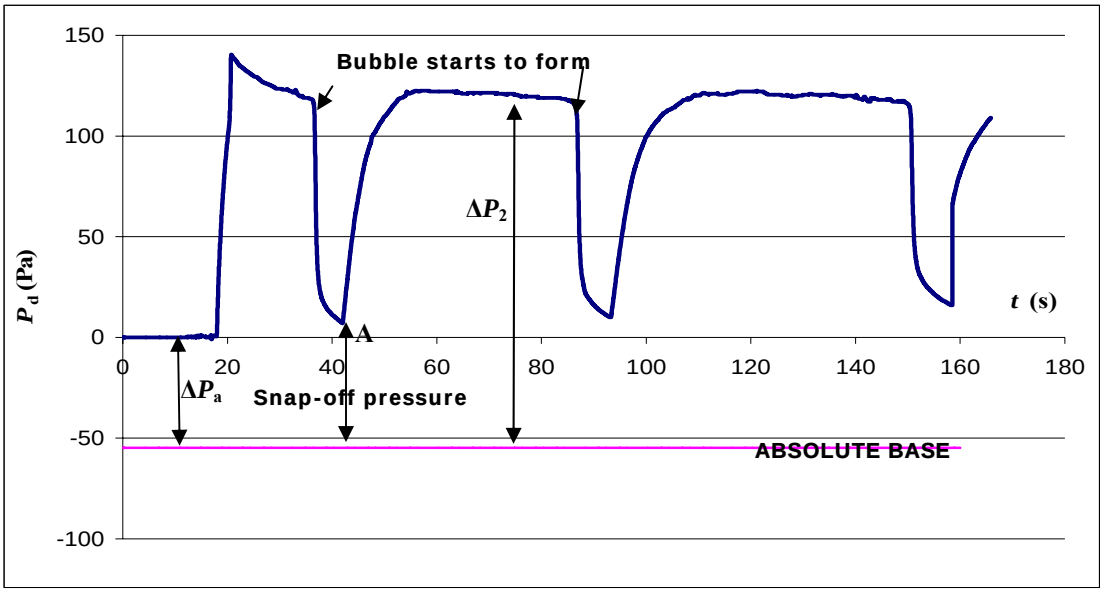

Figure 8-12. Transducer pressure (ΔP_d) recordings at the dead end in the cell during countercurrent flow. The slot angle β is 85º. Negative peaks indicate bubble formation. Once the snap-off is completed, the air pressure regains the initial value and stays almost constant until the next bubble starts to form.

In Figure 8-12, the negative peaks correspond to the onset of bubble formation. The bubble snaps off at the point 'A'. Immediately after snap-off the pressure rises again as the arc menisci shrink back to the curvature of the main meniscus that now advances in the larger tube. This takes a surprisingly long time, mainly because of the considerable resistance to flow in the arc menisci. Little additional imbibition takes place during these local events which are mainly just a rearrangement of fluid. The time between sequential bubbles increases because advance of the meniscus in the smaller capillary slows with time. There are several measurements that can be made from the data pressure plot. The snap-off pressure is equal to the pressure between the absolute base pressure and the snap-off point '*A*'. The pressure difference created by the meniscus in the large tube (ΔP_2) is almost equal to the pressure difference between the absolute base pressure and the pressure that is measured between the formation of bubbles.

When there is a constant capillary back pressure, the imbibition distance varies as $t^{1/2}$, as predicted by the Washburn equation (Washburn, 1921) for cylindrical capillaries. However, when the bubble is forming the imbibition rate increases significantly. The imbibition distance ($x - x_0$) *vs* $t^{1/2}$ for the small capillary during countercurrent flow is shown in Figure 8-13. Note that when a bubble starts to form, the imbibition rate increases and that after snap-off the $t^{1/2}$ relationship is regained. The bumps on Figure 8-13 indicate bubble formation, the slope of the lines between bubble formation are almost the same. Comparison of Figure 12 with Figure 8-13 shows how the pressure change during bubble formation is matched by the increase in imbibition rate. The same data plots during countercurrent flow for the 75° and 65° cells are shown in Figures 8-14 – 8-17.

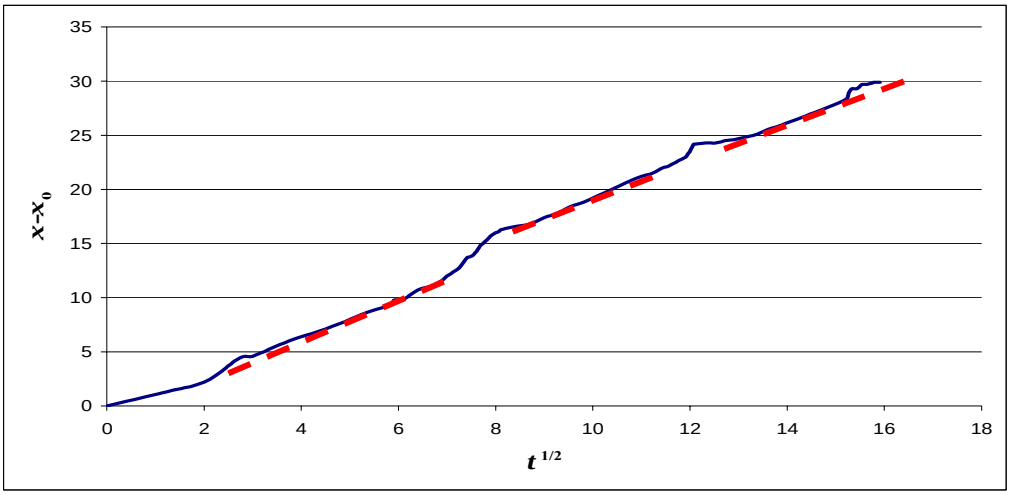

Figure 8-13. The rate of imbibition in the small capillary during countercurrent flow; slot angle β is 85º. The small steps accompany the formation of the bubbles. The dashed lines show that the imbibition rate is almost the same between the bubble formation.

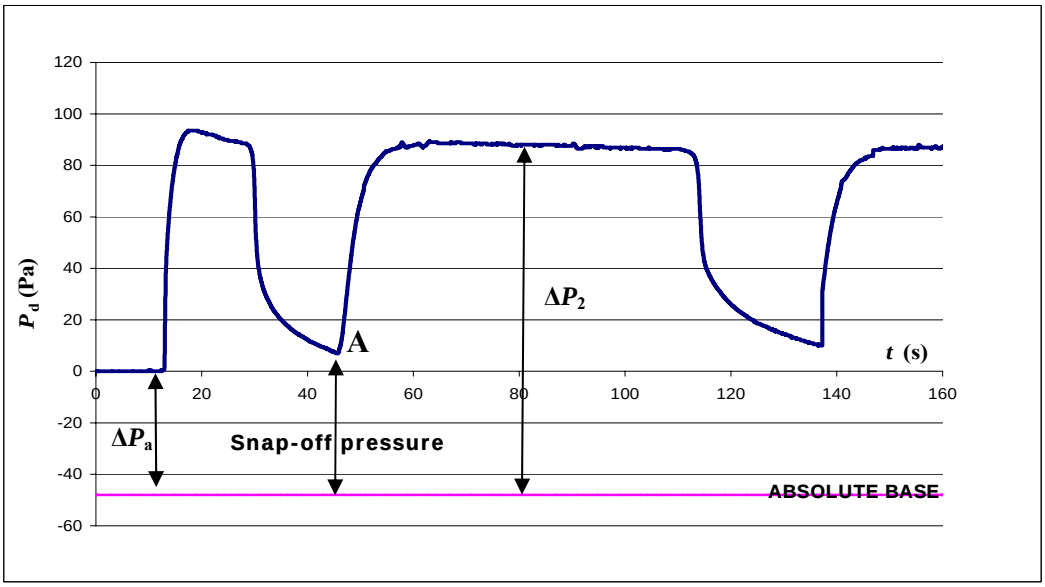

Figure 8-14. Pressure (ΔP_d) recordings in the cell with a slot angle of 75º during countercurrent flow.

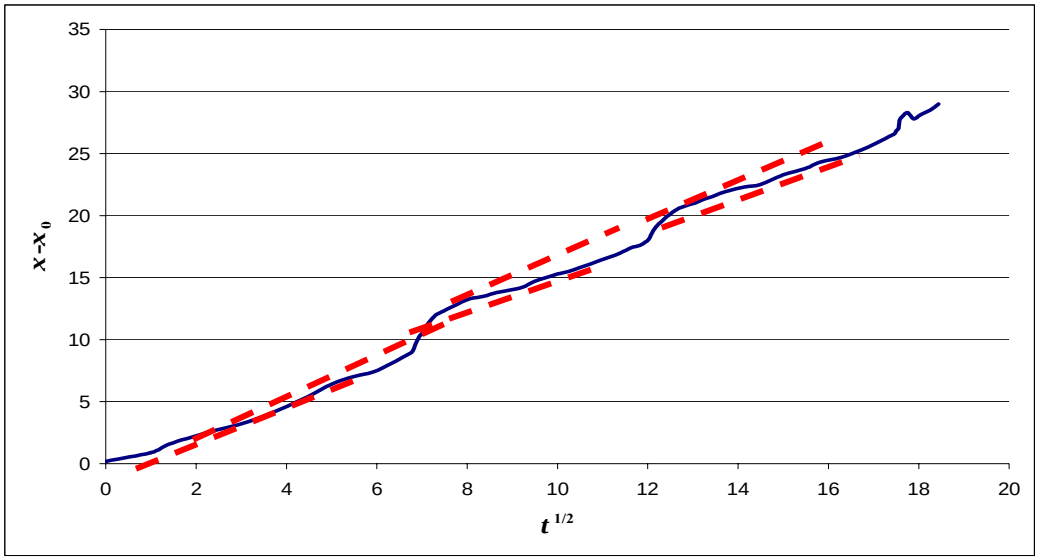

Figure 8-15. The rate of imbibition in the small capillary during countercurrent flow, slot angle is 75º.

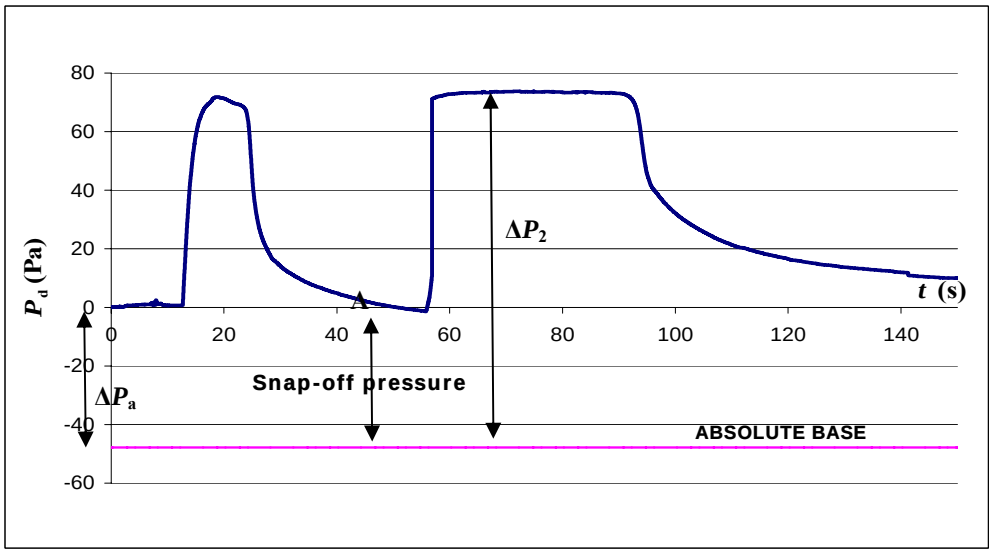

Figure 8-16. Pressure (ΔP_d) recordings in the cell with a slot angle of 65º during countercurrent flow.

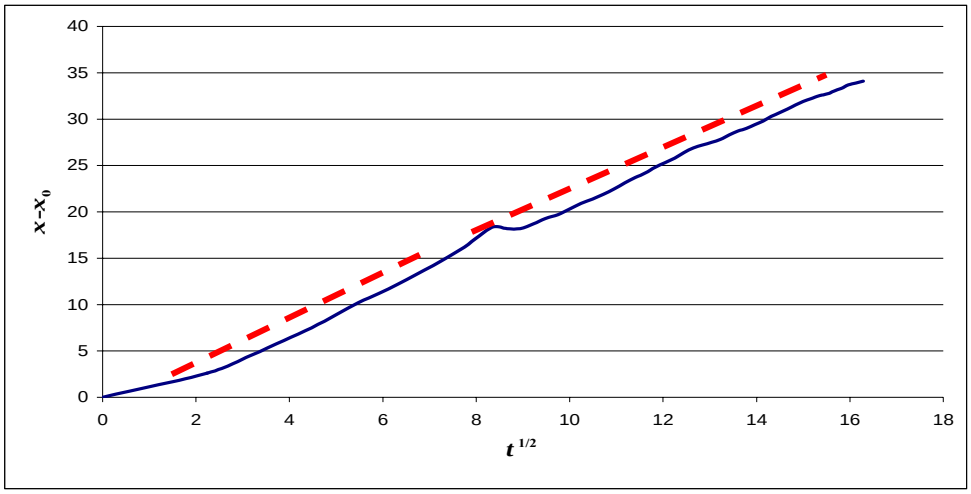

Figure 8-17. The imbibition rate in the small capillary during countercurrent flow; slot angle is 65º. Only one bubble was formed because of the small tube contained so little volume.

The snap-off pressure can be estimated from the incircle that just fits inside the tube (see Figure 8-2). For the 85º cell, the incircle normalized curvature under the condition 'd/R=0' is 5.16. Capillary pressure is related to curvature by

$$\Delta P = \sigma C/R \qquad (8\text{-}26)$$

where ΔP is the capillary pressure, σ is the surface tension, C is the normalized curvature and R is the rod radius. From the incircle, the capillary pressure is calculated as 109 Pa. However, from the graph, the actual pressure for the first bubble is 70 Pa (Figure 8-12). The difference is probably because flow needs to occur for snap-off and a pressure is needed to drive this flow. The pressure at which snap- off occurs therefore depends upon the rate at which the bubble is growing, and this, in turn, depends on the position of the meniscus in the small tube. The effect can be seen in Figure 8-12 where the later bubbles snap off at higher pressures. The snap-off pressure therefore exhibits rate-dependency under dynamic conditions. In addition, the interface is not a perfect uniform cylinder. The measured curvatures are compared with the curvatures obtained from the incircle curvatures in Figure 8-18.

The pressure produced by the meniscus in the large tube (ΔP_2) can be measured from the pressure record during flow. The values for all three cells can be compared with the capillary pressures obtained using capillary rise values (Table 8-2) and using Equation 8-26, where the normalized curvatures are from the MS-P theory (Figure 8-2). It can be seen that they are in excellent agreement (Figure 8-19) indicating that flow does not greatly affect the meniscus curvature predicted by the MS-P theory. To our best knowledge this has not been reported previously in other papers.

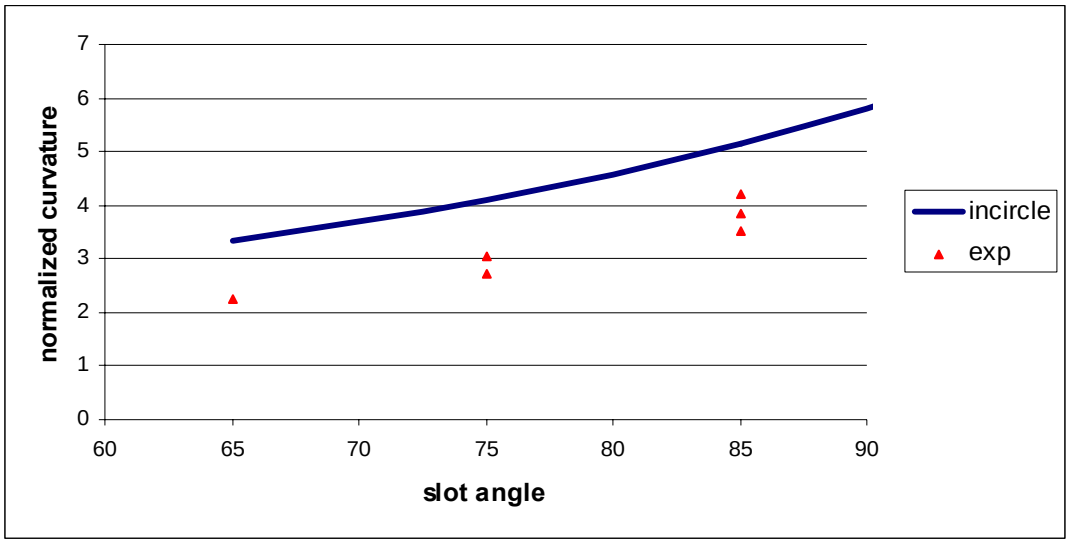

Figure 8-18. Comparison of incircle curvature with snap-off curvature. The snap-off pressures were read from Figures 12, 14 and 16 for the slot angles of 85º (3 bubbles), 75º (2 bubbles) and 65º (1 bubble), respectively.

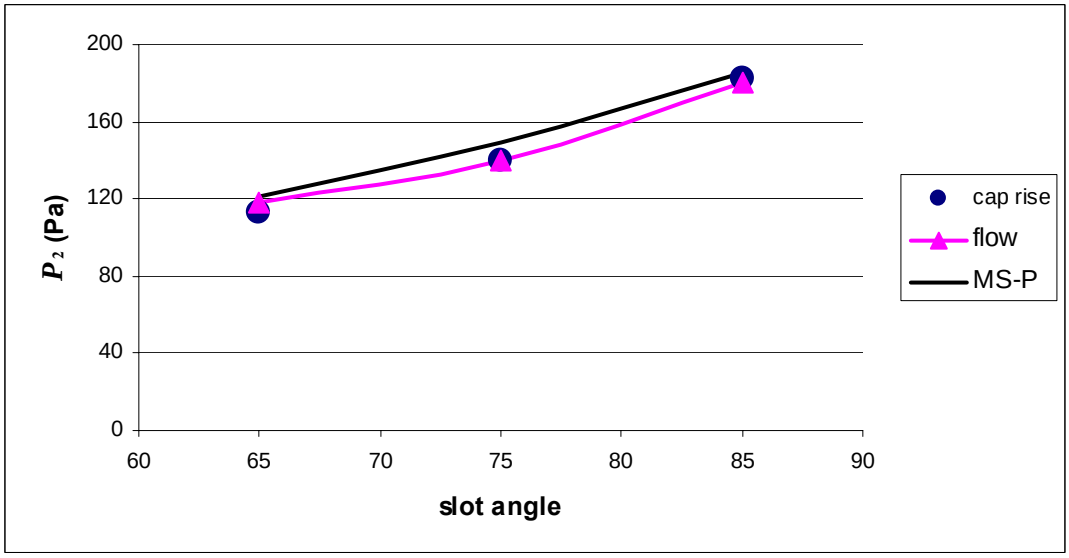

Figure 8-19. Theoretical MS-P and experimental (capillary rise and flow) ΔP_2 values at different slot angles (º).

Equation 8-19 gives the pressure difference between atmosphere and the dead end (ΔP_d) for the constant pressure periods between the release and formation of bubbles. The ΔP_d values were measured as 72 Pa, 90 Pa and 120 Pa for the cells with slot angles 65º, 75º, and 85º respectively (see Figures 8-12, 8-14 and 8-16). Corresponding pressure values from Equation 8-19 are 75 Pa, 103 Pa and 130 Pa. The countercurrent theory presented here only considers the regions between consecutive bubbles, and does not analyze behavior during bubble formation.

Equation 8-20 predicts interface positions during countercurrent imbibition without a bubble being formed. In one series of experiments, imbibition was initially co-current and then the

end was sealed and the imbibition became countercurrent. The B coefficient values were calculated from co-current measurements for all three cells 65º, 75º and 85º as 0.015, 0.078 and 0.35 respectively, while x_1 and x_2 values were determined from the countercurrent video images. Values for A_1 and A_2 were calculated using Equations 8-2 and 8-3, respectively. Following Equation 8-23, $f\left(x_1^2, x_2^2\right)$ vs time were plotted. As expected an almost linear relationship for each cell was obtained (Figure 8-20).

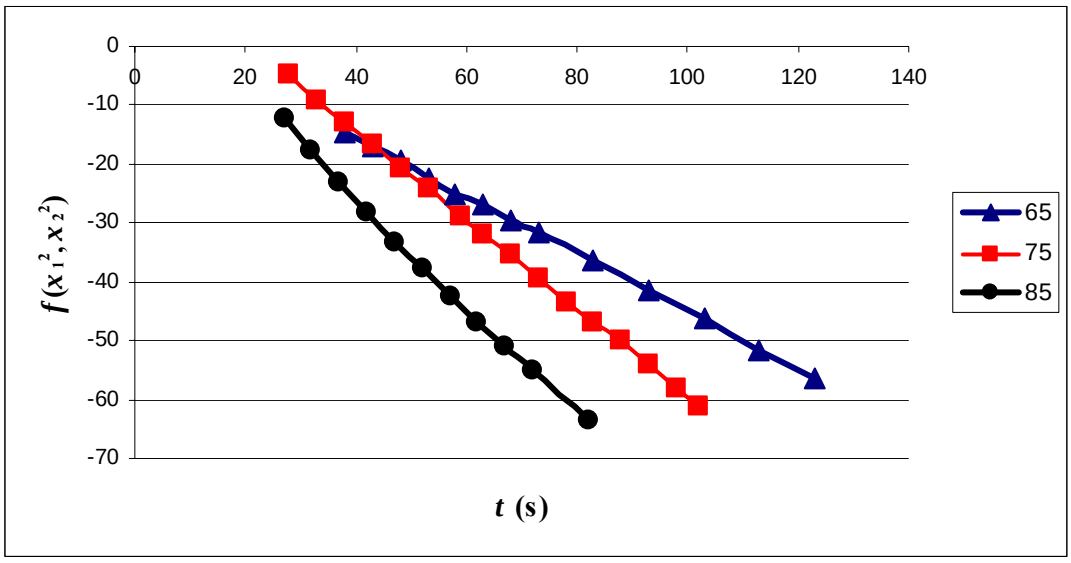

Figure 8-20. Relationship between function of $f\left(x_1^2, x_2^2\right)$ versus time during countercurrent flow for cell with slot angles of 65º, 75º and 85º.

References

Cil, M., J.C. Reis, J. Petroleum Sci. Eng. 16 (1996) 61.

Corey, A.T., Mechanics of Immiscible Fluids in Porous Media, Water Resources Publications, Colorado, 1994.

Dong, M., F.A.L. Dullien, Transp. Porous Media. 27 (1997) 185.

Dong, M., F.A.L. Dullien, J.Zhou, Transp. Porous Media, 31 (1998) 213.

Dong, M., I. Chatzis, J. Colloid Interface Sci. 172 (1995) 278.

Dong, M., F.A.L. Dullien, L. Dai, D. Li, Transp. Porous Media. 59 (2005) 1.

Dong, M., F.A.L. Dullien, L. Dai, D. Li, Transp. Porous Media. 63, (2006) 289.

Dullien, F.A.L., in: V. Kambiz (Eds), Handbook of Porous Media Marcel Dekker, Inc., New York, 2000, p. 53.

Lenormand, R., R., E. Toubul, C. Zarcone, J. Fluid Mech. 189 (1988) 165.

Li, Y., N.R. Morrow, D. Ruth, J. Petroleum Sci. Eng. 39 (2003) 309.

Ma, S., G. Mason, N.R. Morrow, Colloids and Surfaces A: Physicochemical and Engineering Aspects. 117 (1996) 273.

Mason, G., Chem. Eng. J. 38 (1983) 1455.

Mason, G., N.R. Morrow, J. Chem. Soc. Faraday Trans. 80 (1984) 2375.

Mason, G., N.R. Morrow, J. Colloid Interface Sci. 109 (1985) 46.

Mason, G., N.R. Morrow, Proc. R. Soc. London A. 414 (1987) 111.

Mason, G., N.R. Morrow, T.J. Walsh, Studies Surface Sci. Catalysis. 128 (2000) 495.
Mayer, R.P., R.A. Stowe, J. Colloid Interface Sci. 20 (1965) 893.
Nicholson, D., J.H. Petropoulos, J. Physics D: Applied Physics. 4 (1971) 181.
Nicholson, D., J.H. Petropoulos, J. Physics D: Applied Physics. 6 (1973) 1737.
Princen, H.M., J. Colloid Interface Sci. 30 (1969a) 69.
Princen, H.M., J. Colloid Interface Sci. 30 (1969b) 359.
Princen, H.M., J. Colloid Interface Sci. 34 (1970) 171.
Patzek, T.W., J.G. Kristensen, J. Colloid Interface Sci. 236 (2001) 305.
Patzek, T.W., D.B. Silin, J. Colloid Interface Sci. 236 (2001) 295.
Ransohoff, T.C., C.J. Radke, J. Colloid Interface Sci. 172 (1988) 178.
Reis, J.C., M. Cil, J. Petroleum Sci. Eng. 10 (1993) 97.
Ruth, D., J.T. Bartley, J. Proc. 2002 International Symposium of the Society of Core Analysts, Monterey, California, SCA2002-05, (2003) 12.
Sisavath, S., X. Jing, R.W, Zimmerman, Transp. Porous Media. 45 (2001) 41.
Washburn, E.W., The Physical Review. 17 (1921) 273.
Walsh, T.J., "Capillary properties of model pores". PhD Thesis, Loughborough University of Technology, 1989.

Task 9. *Increased oil recovery by spontaneous imbibition.*

The methods described under Task 6 are now being adapted to measure the buble pressures for oil production. The effect of reduction of bubble pressure on oil production rate by means of surfactants and other controlled methods of lowering interfacial tension will be tested. Further tests and variation of brine composition on use of surfactants to improve oil recovery are in progress.

CONCLUSIONS

Task 6

- Pressures in the oil phase ahead of the imbibition front (end pressures) for restricted countercurrent spontaneous imbibition have been determined for a range of conditions. These novel measurements include strongly water wet cores with and without initial water saturation, mixed wet cores with different levels of initial water saturation, and cores initially saturated with crude oil.

- Strongly water wet cores showed decrease in end pressure with increase in initial water saturation consistent with decrease in the capillary driving force.

- In contrast to water wet conditions, mixed wet cores showed increase in driving pressure with increase in initial water saturation. This result is consistent with the effect of aging on the available surface energy for imbibition and with standard imbibition tests on mixed wet rocks having a range of initial water saturations.

- Measured pressures stayed close to constant until the imbibition front reached the end of the core sample.

Task 7

- An analytic solution for imbibition has been developed by approximating the countercurrent imbibition process to a frontal displacement with constant saturations ahead of and behind the front, and taking the capillary back pressure at the open face to be a constant fraction of the capillary pressure at the front. This gives the production *vs* time functions for different core shapes. Comparison of these functions with experimental data using Berea sandstone and refined oil for both the linear and radial cases shows reasonable agreement. Variability between the cores caused by not having enough surface area and not enough volume seems of greater importance than the precise core scale factor functions.

Task 8.

- A simple analysis of co- and countercurrent imbibition for tubes of non-circular cross-section has been carried out. Shape factors were needed to describe the tube areas, hydraulic resistances and capillary pressures. Experiments using model pore systems and measurements of capillary rise were used to confirm the capillary pressures. Co-current imbibition experiments were used to measure the hydraulic resistances. Both these values were then used to quantify countercurrent imbibition. When theory was compared to experiment, the agreement was generally good

- In general, co-current imbibition was observed to occur at about four times the rate of countercurrent imbibition. Furthermore, it takes a significant positive pressure, the capillary back pressure, for air to be driven out in countercurrent imbibition and this can make a significant difference to the imbibition rate. At the liquid inlet face there was growth of bubbles and subsequent snap-off giving significant fluctuations of the capillary back pressure. Co-current theory was in good agreement with the experiments.

- The Mayor & Stowe –Princen theory appears to predict meniscus curvatures well, even when they are moving. This is probably because the arc menisci keep far enough ahead of the main terminal meniscus for the MS-P approximations to hold.